INTERNATIONAL JOURNAL FOR NUMERICAL METHODS IN FLUIDS
Int. J. Numer. Meth. Fluids 2005; **49**:657–699
Published online 21 July 2005 in Wiley InterScience (www.interscience.wiley.com). DOI: 10.1002/fld.1005

A local-analytic-based discretization procedure for the numerical solution of incompressible flows

J. P. Pontaza[1,*,†], H. C. Chen[2,‡] and J. N. Reddy[1,§]

[1]*Department of Mechanical Engineering, Texas A&M University, College Station, TX 77843-3123, U.S.A.*
[2]*Department of Civil Engineering, Texas A&M University, College Station, TX 77843-3123, U.S.A.*

SUMMARY

We present a local-analytic-based discretization procedure for the numerical solution of viscous fluid flows governed by the incompressible Navier–Stokes equations. The general procedure consists of building local interpolants obtained from local analytic solutions of the linear multi-dimensional advection–diffusion equation, prototypical of the linearized momentum equations. In view of the local analytic behaviour, the resulting computational stencil and coefficient values are functions of the local flow conditions. The velocity–pressure coupling is achieved by a discrete projection method. Numerical examples in the form of well-established verification and validation benchmarks are presented to demonstrate the capabilities of the formulation. The discretization procedure is implemented alongside the ability to treat embedded and non-matching grids with relative motion. Of interest are flows at high Reynolds number, $\mathcal{O}(10^5)-\mathcal{O}(10^7)$, for which the formulation is found to be robust. Applications include flow past a circular cylinder undergoing vortex-induced vibrations (VIV) at high Reynolds number. Copyright © 2005 John Wiley & Sons, Ltd.

KEY WORDS: local-analytic-based discretization; viscous incompressible fluid flows; high Reynolds number flows; VIV at high Reynolds number

1. INTRODUCTION

1.1. Background

During the past three decades considerable efforts have been directed towards the development of robust computational procedures for fluid flow problems. Predominantly, fluid flow

*Correspondence to: Juan P. Pontaza, Department of Mechanical Engineering, Texas A&M University, College Station, TX 77843-3123, U.S.A.
†E-mail: pontaza@tamu.edu
‡E-mail: hcchen@civil.tamu.edu
§E-mail: jnreddy@shakti.tamu.edu

Contract/grant sponsor: Offshore Technology Research Center
Contract/grant sponsor: Department of Interior, Mineral Management Services

Received 21 July 2004
Revised 19 April 2005
Accepted 24 April 2005

Copyright © 2005 John Wiley & Sons, Ltd.

analyses are being performed using finite-difference methods with body-fitted coordinate transformations and control-volume methods [1], the latter being a low-order weighted residual method for approximating the solution via local conservation. However, increasingly, finite element formulations using low-order and high-order polynomial approximation spaces are being used [2, 3].

In the finite element solution of fluid flows, using the Bubnov–Galerkin formulation in which the test and trial functions are the same, inappropriate discretization of the convection terms is a source of potential numerical instabilities. The Bubnov–Galerkin formulation treats the convection term symmetrically, which can result in spurious node-to-node oscillations if the discretization scale is too large to resolve sub-grid phenomena, in particular boundary layers. Such oscillations become significant as the Reynolds number increases. They can be suppressed by refining the mesh or increasing the order of the approximation space, but the necessary degree of refinement is often prohibitively expensive. This numerical instability is not unique to finite element discretizations, and is also present in finite-difference- and control-volume-type discretizations.

In the context of finite elements, various procedures have been proposed to eliminate this numerical instability, starting in the 1970s when Christie *et al.* [4] proposed a stable scheme for the one-dimensional, steady-state advection–diffusion equation without source terms. The stabilization was controlled to give the analytic nodal solution for the one-dimensional case. The scheme was based on the Petrov–Galerkin formulation, in which the trial and test functions are different and the test functions would give more weight to upstream nodes. Shortly after, Heinrich *et al.* [5] proposed a two-dimensional scheme, which was a straightforward extension of Christie's earlier work. The scheme applied one-dimensional stabilization along the edges of the two-dimensional element. However, several difficulties were encountered with this generalization of the scheme to multi-dimensions. These were attributed to cross-wind diffusion, which manifests itself when the flow is skewed to the mesh lines. Moreover, when the scheme was applied to more complicated situations (transient problems and/or when source terms were present) it was found to be far from optimal, and in many instances the Bubnov–Galerkin formulation would give more accurate results [6].

In the 1980s Brooks and Hughes [6] introduced the SUPG (streamline upwind Petrov–Galerkin) scheme for piecewise linear elements, which reduced the oscillations by adding an artificial diffusion term in the streamline direction. Later, Hughes *et al.* [7] generalized the formulation by adding the least-squares form of residuals to the Galerkin formulation. These approaches have failed to achieve widespread use and acceptance due to their explicit dependence on various mesh-dependent calibration parameters that need to be fine-tuned from application to application.

Recently, least-squares-based finite element formulations using low- and high-order approximation spaces have shown to be robust for the numerical solution of viscous fluid flow problems [8–10]. However, unlike weak form Galerkin formulations, where the smoothness requirements of the finite element spaces are weakened by the integration by parts step, least-squares formulations have associated with them the requirement of higher smoothness—dictated by the differentiability requirements of the governing equation(s) under consideration and the norms used to measure the residuals in the least-squares functional. The *higher smoothness* requirement is considered the *major drawback* of least-squares-based formulations and is one of the reasons why the methodology has not yet gained widespread acceptance. In modern implementations of the formulation, the higher smoothness requirement is bypassed by

Copyright © 2005 John Wiley & Sons, Ltd.

introducing auxiliary variables to recast the governing equations and re-formulate the problem as a set of first-order equations. Yet another concern, not easily remedied, is that the resulting discrete system is quite sensitive to small changes in Reynolds number, as the parameter $(1/Re)$ appears as $(1/Re)^2$ in the discrete equations [11]. Thus, the formulation in its traditional form seems to be not well suited for the solution of high Reynolds number flow.

1.2. Present work

The objective of this work is to present a novel discretization procedure, where interpolants for the velocity components are obtained from local analytic solutions of the locally linearized momentum equations, i.e. local non-homogeneous constant-coefficient advection–diffusion equations. The procedures are described in detail for the two-dimensional case, and the extension to the three-dimensional case is outlined.

The local analytic solution is obtained for rectangular shaped elements by constructing appropriate boundary data satisfying the natural solution and using the method of separation of variables. The resulting interpolants have zeroth- and first-order consistency and are functions of the local flow conditions, with the ability to respond analytically to flow vectors skew to the element boundaries. For the general case of geometrically distorted or curvilinear elements, the interpolants are constructed in the bi-unit square and mapped back to the physical space. An inherent limitation of the formulation, is that it is only possible to construct the interpolants in structured meshes. Thus, the formulation is implemented with overset grid capabilities, allowing the use of embedded and non-matching structured grids to represent complex geometries, and allowing for the possibility of relative grid motions.

The interpolants may be used as a polynomial interpolant would be used, in a weak form Galerkin formulation or a least-squares formulation. However, the interpolants are rational functions and are not easily differentiated or integrated. To arrive at a fast and efficient formulation, we adopt a collocation-type formulation whereby the interpolant is evaluated at the centre of the element and provides a stencil relating its neighbours. The resulting computational stencil and coefficient values are functions of the local flow conditions and retain the ability to respond to flow vectors skew to the element boundaries. The expressions for the computational stencil were first documented by Chen [12] and Chen and Chen [13], where they were coined as the 'finite analytic coefficients' due to their local analytic behaviour, and used to discretize the Navier–Stokes equations in their stream function-vorticity form.

An overview of the paper is as follows. In Section 2, we present the governing equations and in Section 3, details on the two-dimensional local analytic interpolants. Section 4, presents details on the adopted collocation-type formulation, the pressure–velocity coupling approach via a discrete projection method, and the overall numerical solution strategy. Section 5 is devoted to numerical examples in the form of verification and validation benchmarks, which include among others, flow over a backward-facing step, flow past a circular cylinder, and three-dimensional lid-driven cavity flows. In Section 6 we present a summary and concluding remarks.

2. GOVERNING EQUATIONS

Let $\bar{\Omega}$ be the closure of an open bounded region Ω in $\mathbb{R}^d$, where $d=2$ or 3 represents the number of space dimensions, and $\mathbf{x}=(x_1,\ldots,x_d)=(x,y,z)$ be a point in $\bar{\Omega}=\Omega\cup\partial\Omega$,

Copyright © 2005 John Wiley & Sons, Ltd.

where $\partial\Omega = \Gamma$ is the boundary of Ω. We consider the solution of the Navier–Stokes equations governing viscous incompressible flow, which in dimensionless form can be stated as follows:

Find the velocity $\mathbf{u}(\mathbf{x}, t)$ and pressure $p(\mathbf{x}, t)$ such that

$$\frac{\partial \mathbf{u}}{\partial t} + (\mathbf{u} \cdot \nabla)\mathbf{u} + \nabla p - \frac{1}{Re} \nabla \cdot [(\nabla \mathbf{u}) + (\nabla \mathbf{u})^{\mathrm{T}}] = \mathbf{f} \quad \text{in } \Omega \times (0, \tau] \tag{1}$$

$$\nabla \cdot \mathbf{u} = 0 \quad \text{in } \Omega \times (0, \tau] \tag{2}$$

$$\mathbf{u}(\mathbf{x}, 0) = {}^0\mathbf{u}(\mathbf{x}) \quad \text{in } \Omega \tag{3}$$

$$\mathbf{u} = \mathbf{u}^s \quad \text{on } \Gamma_u \times (0, \tau] \tag{4}$$

$$\hat{\mathbf{n}} \cdot \boldsymbol{\sigma} = \mathbf{f}^s \quad \text{on } \Gamma_f \times (0, \tau] \tag{5}$$

where $\Gamma = \Gamma_u \cup \Gamma_f$ and $\Gamma_u \cap \Gamma_f = \emptyset$, τ is a real number (time) > 0, Re is the Reynolds number, $\nabla \cdot {}^0\mathbf{u} = 0$, $\boldsymbol{\sigma} = -p\,\mathbf{I} + 1/Re\,[(\nabla \mathbf{u}) + (\nabla \mathbf{u})^{\mathrm{T}}]$, $\mathbf{f}$ is a dimensionless force, $\hat{\mathbf{n}}$ is the outward unit normal on the boundary of Ω, $\mathbf{u}^s$ is the prescribed velocity on the boundary Γ_u, $\mathbf{f}^s$ are the prescribed tractions on the boundary Γ_f, and in Equation (4) the initial conditions are given. We assume the problem is well posed.

In this work we prefer to use the Navier–Stokes equations in the $\nabla^2\mathbf{u}$ form. Using the incompressibility constraint given in Equation (2) we drop the $(\nabla \mathbf{u})^{\mathrm{T}}$ term in Equation (1), and the boundary conditions in Equation (5) then become

$$\hat{\mathbf{n}} \cdot \tilde{\boldsymbol{\sigma}} = \tilde{\mathbf{f}}^s \quad \text{on } \Gamma_f \times (0, \tau] \tag{6}$$

where $\tilde{\boldsymbol{\sigma}}$ is a pseudo-stress, $\tilde{\boldsymbol{\sigma}} = -p\,\mathbf{I} + (1/Re)\,\nabla \mathbf{u}$, and $\tilde{\mathbf{f}}^s$ are the prescribed pseudo-tractions on the boundary Γ_f, prescribed as zero at an outflow boundary. In situations where outflow boundary conditions need to be modelled, Equation (6) has been reported and documented to perform satisfactorily [14].

3. TWO-DIMENSIONAL LOCAL ANALYTIC INTERPOLANTS

We start by decomposing $\bar{\Omega} \subset \mathbb{R}^2$ into non-overlapping elements, $\bar{\Omega}_e$, such that

$$\bar{\Omega} \approx \bar{\Omega}^h = \bigcup_{e=1}^{E} \bar{\Omega}_e$$

where the region $\bar{\Omega}^h$ is called the connected model or discretization of $\bar{\Omega}$.

In the connected model, we identify a finite number G of points, called *global nodes*, and we label them consecutively $\mathbf{x}^1, \mathbf{x}^2, \ldots, \mathbf{x}^G$. Likewise, we identify within each element $\bar{\Omega}_e$ a number of N_e points, called *local nodes*, and we label them consecutively $\mathbf{x}_e^1, \mathbf{x}_e^2, \ldots, \mathbf{x}_e^{N_e}$; $e = 1, 2, \ldots, E$. A correspondence must exist between points in $\bar{\Omega}_e$ and $\bar{\Omega}^h$, in particular, between nodal points $\mathbf{x}_e^n$ in $\bar{\Omega}_e$ and nodes $\mathbf{x}^i$ in $\bar{\Omega}^h$, if the elements are to fit together smoothly to form $\bar{\Omega}^h$.

Let $\mathscr{P}_h = \{\mathscr{Q}\}$ be a family of quadrilateral finite elements $\bar{\Omega}_e$ that make up the connected model $\bar{\Omega}^h$. We consider the special case where $\mathscr{P}_h$ consists of rectangles. Consider one such

Copyright © 2005 John Wiley & Sons, Ltd.

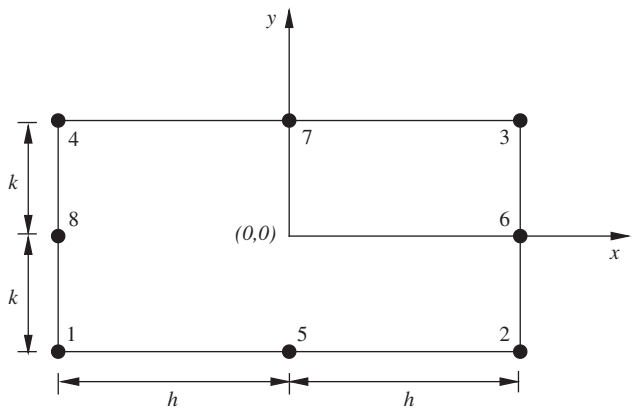

Figure 1. Rectangular element, $\bar{\Omega}_e$, of dimensions $[-h,h]\times[-k,k]$ with 8 boundary nodes.

rectangle $\bar{\Omega}_e = \mathscr{Q}$ and let $\mathbf{x} = (x_1, x_2) = (x, y)$ be a point in $\bar{\Omega}_e$. Furthermore, let us give the rectangle dimensions $-h \leqslant x \leqslant h$ and $-k \leqslant y \leqslant k$, as shown in Figure 1.

We take the linear advection–diffusion equation, which is prototypical of the linearized momentum equations, as our model equation and obtain a local analytic solution for the case of two-dimensional flow. Consider the linear advection–diffusion equation in dimensionless form

$$\mathbf{u}\cdot\nabla\theta - \frac{1}{Pe}\nabla^2\theta = f \quad \text{in } \Omega_e \tag{7}$$

where $\theta(\mathbf{x})$ is the transported scalar, Pe is the Peclet number, and both the velocity field $\mathbf{u} = (u_1, u_2)$ and the right-hand side f are prescribed and piecewise constant with respect to the tessellation $\mathscr{P}_h$.

By imposing suitable boundary functions on $\partial\Omega_e = \Gamma_e$, a local analytic solution is readily obtained by using the method of separation of variables. The natural solution of Equation (7) suggests that a combination of exponential and linear boundary functions on all four boundaries of the rectangle be specified (see Appendix A for details). For example, at $y = k$ and $x = h$, the boundary functions are of the form

$$\theta(x) = a_{\mathrm{N}}(\mathrm{e}^{2Ax} - 1) + b_{\mathrm{N}}x + c_{\mathrm{N}} \tag{8}$$

$$\theta(y) = a_{\mathrm{E}}(\mathrm{e}^{2By} - 1) + b_{\mathrm{E}}y + c_{\mathrm{E}} \tag{9}$$

with

$$2A = (Pe)u_1 \quad \text{and} \quad 2B = (Pe)u_2 \tag{10}$$

The boundary functions suggest that a total of eight nodes, $N_e = 8$, should be placed on the boundary of the rectangle $\mathscr{Q}$, as shown in Figure 1, and the coefficients $a_{\mathrm{N}}, b_{\mathrm{N}}, c_{\mathrm{N}}, a_{\mathrm{E}}, \ldots$, etc., parametrized in terms of nodal variables $\{\theta_n\}_{n=1}^{8}$.

Copyright © 2005 John Wiley & Sons, Ltd.

In the limit of absent advection ($A \to 0, B \to 0$), the boundary functions can be shown to recover the quadratic form

$$\theta(x) = \hat{a}_{\mathrm{N}} x^2 + \hat{b}_{\mathrm{N}} x + c_{\mathrm{N}}$$

$$\theta(y) = \hat{a}_{\mathrm{E}} y^2 + \hat{b}_{\mathrm{E}} y + c_{\mathrm{E}}$$

where the parametrized coefficients $\hat{a}_{\mathrm{N}}, \hat{a}_{\mathrm{E}}, \ldots$, are automatically recovered from the coefficients $a_{\mathrm{N}}, a_{\mathrm{E}}, \ldots$, by considering the limit $A \to 0, B \to 0$. In this limit the local analytic solution would correspond to that of a Poisson problem. This is an important observation and implies that locally partially parabolic flows (e.g. $A \neq 0$, $B \to 0$) can be automatically represented.

With the specification of the boundary functions, Equation (7) can be solved analytically by the method of separation of variables to obtain functions (or interpolants) $\{\alpha_n(\mathbf{x})\}_{n=1}^{8}$, $\alpha_f(\mathbf{x})$ such that

$$\theta(\mathbf{x}) = \sum_{n=1}^{8} \alpha_n(\mathbf{x})\theta_n + \alpha_f(\mathbf{x}) f \quad \text{in } \Omega_e \tag{11}$$

The local analytic interpolants $\{\alpha_n(\mathbf{x})\}_{n=1}^{8}$, $\alpha_f(\mathbf{x})$ are functions of the geometry of the element Ω_e, the velocity field $\mathbf{u}$, and the Peclet number. Details of the solution procedure by the method of separation of variables are given in Appendix A.

The interpolants $\{\alpha_n(\mathbf{x})\}_{n=1}^{8}$, have zeroth-order consistency (implying $\sum_{n=1}^{8} \alpha_n(\mathbf{x}) = 1$), first-order consistency, and are always positive. In view of the latter property and the zeroth-order consistency, they are bounded: $0 \leqslant \{\alpha_n(\mathbf{x})\}_{n=1}^{8} \leqslant 1$.

In addition to zeroth- and first-order consistency, the interpolants $\{\alpha_n(\mathbf{x})\}_{n=1}^{8}$ are able to represent higher-order modes. However, this is difficult to show explicitly due to their complicated functional form—but can be shown to exist through numerical verification benchmarks. In such tests, the interpolation error displays a $\mathcal{O}(h^4)$ convergence rate, indicating the existence of higher-order consistency.

When evaluated at $\mathbf{x} = (0,0)$, the coefficients $\{\alpha_n(\mathbf{0})\}_{n=1}^{8} = \{\alpha_n^0\}_{n=1}^{8}$, $\alpha_f(\mathbf{0}) = \alpha_f^0$ are

$$\begin{aligned} \alpha_1^0 &= \mathrm{e}^{Ah+Bk} D_0, & \alpha_5^0 &= \mathrm{e}^{Bk} D_1 \\ \alpha_2^0 &= \mathrm{e}^{-Ah+Bk} D_0, & \alpha_6^0 &= \mathrm{e}^{-Ah} D_2 \\ \alpha_3^0 &= \mathrm{e}^{-Ah-Bk} D_0, & \alpha_7^0 &= \mathrm{e}^{-Bk} D_1 \\ \alpha_4^0 &= \mathrm{e}^{Ah-Bk} D_0, & \alpha_8^0 &= \mathrm{e}^{Ah} D_2 \end{aligned} \tag{12}$$

$$\alpha_f^0 = \frac{Pe}{2(A^2+B^2)} \{Ah \tanh Ah + Bk \tanh Bk - 4 \cosh Ah \cosh Bk [(Ah)^2 E_2 + (Bk)^2 E_2']\} \tag{13}$$

with

$$D_0 = \tfrac{1}{2}(E_1 + E_1') - Ah \coth Ah E_2 - Bk \coth Bk E_2' \tag{14}$$

$$D_1 = 2Ah \coth Ah \cosh Ah E_2 \tag{15}$$

$$D_2 = 2Bk \coth Bk \cosh Bk E_2' \tag{16}$$

Copyright © 2005 John Wiley & Sons, Ltd.

where E_1, E_2, E_1', and E_2' are infinite series

$$E_i = \sum_{m=1}^{\infty} \frac{-(-1)^m(\lambda_m^h h)}{[(Ah)^2 + (\lambda_m^h h)^2]^i} \left(\frac{1}{\cosh(\mu_m^h k)} \right) \tag{17}$$

with

$$\lambda_m^h = \frac{(2m-1)\pi}{2h}, \quad \mu_m^h = \sqrt{A^2 + B^2 + (\lambda_m^h)^2}$$

and similarly

$$E_i' = \sum_{m=1}^{\infty} \frac{-(-1)^m(\lambda_m^k k)}{[(Bk)^2 + (\lambda_m^k k)^2]^i} \left(\frac{1}{\cosh(\mu_m^k h)} \right) \tag{18}$$

with

$$\lambda_m^k = \frac{(2m-1)\pi}{2k}, \quad \mu_m^k = \sqrt{A^2 + B^2 + (\lambda_m^k)^2}$$

By explicitly enforcing zeroth- and first-order consistency on $\{\alpha_n^0\}_{n=1}^8$, we are able to express functions of the infinite series analytically:

$$\frac{1}{2}(E_1 + E_1') = \frac{1}{4\cosh Ah \cosh Bk} \tag{19}$$

$$E_2' - E_2 \left(\frac{h}{k} \right)^2 = \frac{Ak \tanh Bk - Bh \tanh Ah}{4AkBk \cosh Ah \cosh Bk} \tag{20}$$

In view of definition (14) and relationship (19), we see that the summation series E_1 and E_1' need not be evaluated. In addition, in view of Equation (20), relating summation series E_2 and E_2', we see that only one such series need be evaluated—thus significantly reducing the computational effort when evaluating the coefficients. The rate of convergence of either series is a function of the element aspect ratio and local flow conditions, however, taking the first twelve terms is generally sufficient.

At this point we wish to point out and make clear that the interpolants $\{\alpha_n(\mathbf{x})\}_{n=1}^8$ are *not* tensor products of the boundary functions given by Equations (8) and (9). They are obtained by analytically solving problem (7) augmented with boundary conditions of the form (8) and (9). The tensor product approach has been investigated in Reference [15], and cannot be categorized as a local-analytic-based approach as the tensor product interpolants do not satisfy Equation (7).

Evaluation of the local analytic interpolants $\{\alpha_n(\mathbf{x})\}$ at other points besides $\mathbf{x} = (0,0)$ requires the evaluation of additional infinite series, which become computationally expensive and/or numerically ill-conditioned due to accumulation of roundoff error. To reduce computational costs and/or avoid the evaluation of numerical ill-conditioned series we devise an approximation strategy whereby the coordinate axes in Figure 1 are translated to the desired evaluation point and the evaluation carried out in terms of the coefficients $\{\alpha_n^0\}_{n=1}^8$ with suitable modifications.

Plots illustrating the behaviour of $\alpha_8(\mathbf{x})$ in a bi-unit square for different values of cell Reynolds number, Ah and Bk, are shown in Figure 2. Figure 2(a) shows the limit case of

Copyright © 2005 John Wiley & Sons, Ltd.

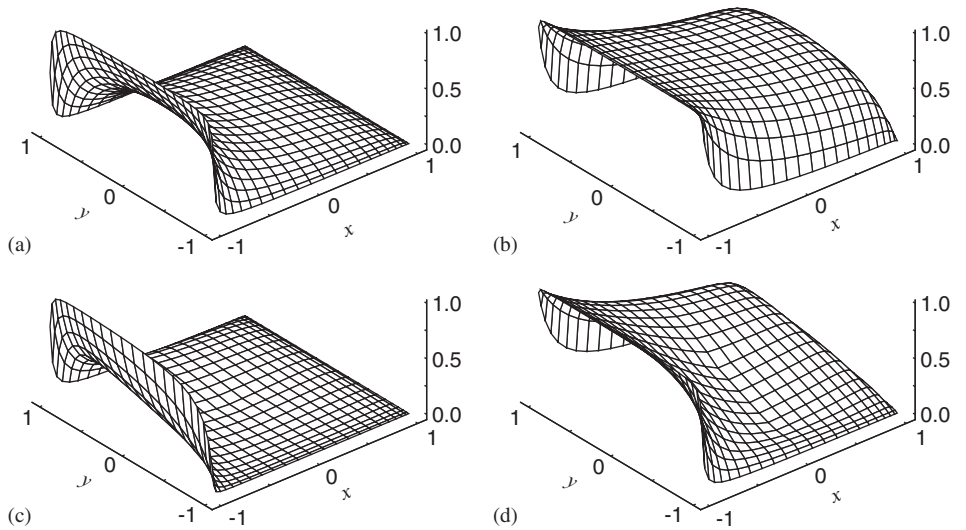

Figure 2. $\alpha_8(\mathbf{x})$ for different values of Ah and Bk. (a) The case of $Ah, Bk \to 0$ is that of pure diffusion. In (b) convection is present, flow is strictly in the positive x direction, $Ah = 5$, $Bk \to 0$. In (c) flow is strictly in the positive y direction, $Ah \to 0$, $Bk = 5$. In (d) convection is present in the positive x and y directions, flow at a 30° angle from the x-axis, $Ah = 2\sqrt{3}$, $Bk = 2$.

pure diffusion. In Figure 2(b) convection is present, flow is in the positive x direction. Note how the function $\alpha_8(\mathbf{x})$ responds to the flow conditions, the solution at any point inside the bi-unit square will have a strong dependence from the upstream value θ_8. Figure 2(c) shows the case of flow in the positive y direction, in this scenario θ_8 will have little or no contribution to the solution inside the bi-unit square. Figure 2(d) shows the function's response to flow at an angle. We can see that the function responds appropriately to the skewed velocity vector.

From Figure 2, we note that the functions fail to recover the imposed boundary functions. This is due to the approximation strategy used to evaluate the interpolants at any other points besides $\mathbf{x} = (0, 0)$. However, we shall not concern ourselves with this issue here, as we will adopt a collocation-type procedure for which evaluation of the local analytic interpolants is only needed at $\mathbf{x} = (0, 0)$. We refer the interested reader to Reference [15], where details of the axes translation approximation scheme are given and where the issue on how to recover the boundary functions is addressed. Details on how to differentiate and integrate the local analytic interpolants, and how to use them to develop a weak form Galerkin finite element model for the incompressible Navier–Stokes equations may also be found in Reference [15].

In practical implementations $\mathscr{P}_h$ will seldom consist of rectangles. In some areas or throughout the entire connected model the quadrilaterals may be geometrically skewed, e.g. when using body-fitted non-orthogonal meshes. We proceed by mapping $\bar{\Omega}_e$ to a bi-unit square $\hat{\Omega}_e = [-1, 1] \times [-1, 1]$, where $\boldsymbol{\xi} = (\xi_1, \xi_2) = (\xi, \eta)$ is a point in $\hat{\Omega}_e$, and construct the local analytic interpolants in $\hat{\Omega}_e$. In this new coordinate system Equations (12) and (13) still apply, with the following new definitions:

$$A = \frac{c_1}{\sqrt{g^{11}}} \quad \text{and} \quad B = \frac{c_2}{\sqrt{g^{22}}} \tag{21}$$

Copyright © 2005 John Wiley & Sons, Ltd.

with

$$2c_i = Pe\,\frac{\partial \xi_i}{\partial x_j}\,u_j - \frac{1}{J}\,\frac{\partial}{\partial \xi_k}\,(Jg^{ik}) \tag{22}$$

where g^{ij} is the contravariant metric tensor and J is the Jacobian associated with the mapping, $\bar{\Omega}_e \rightleftarrows \hat{\Omega}_e$. Also, h and k are to be replaced by $1/\sqrt{g^{11}}$ and $1/\sqrt{g^{22}}$ when used in Equations (12) and (13). Details of the transformation are given in Appendix B.

4. LOCAL ANALYTIC DISCRETIZATION OF THE NAVIER–STOKES EQUATIONS

4.1. Discretization of the momentum equations

The advection–diffusion equation and the momentum equations are similar in form:

$$\frac{\partial \theta}{\partial t} + \mathbf{u}\cdot\nabla\theta - \frac{1}{Pe}\,\nabla^2\theta = f \tag{23}$$

$$\frac{\partial \mathbf{u}}{\partial t} + (\mathbf{u}\cdot\nabla)\mathbf{u} - \frac{1}{Re}\,\nabla^2\mathbf{u} = \mathbf{f} - \nabla p \tag{24}$$

and Equation (11) can be used to develop discretization procedures.

Here, we adopt a collocation-type procedure, where an interior node is placed at $\mathbf{x} = (0,0)$ in element ② of Figure 1 and Equation (11) is evaluated at the interior node. The resulting coefficients, given by Equations (12) and (13) with the Peclet number replaced by the Reynolds number, are used to construct a stencil relating nine nodal variables. Using a backward Euler representation of the temporal terms, and denoting the discrete pressure gradient by $\nabla_h p$, we arrive at the discretized momentum equations

$$\alpha_f^0\,\frac{{}^{t+\Delta t}\mathbf{u}^0 - {}^{t}\mathbf{u}^0}{\Delta t} + \left\{ {}^{t+\Delta t}\mathbf{u}^0 - \sum_{n=1}^{8} \alpha_n^0\,{}^{t+\Delta t}\mathbf{u}_n \right\} = \alpha_f^0 [{}^{t+\Delta t}\mathbf{f}^0 - {}^{t+\Delta t}(\nabla_h\, p)^0] \tag{25}$$

where the superscript '0' denotes that the quantity under consideration is evaluated at the interior node located at $\mathbf{x} = (0,0)$ in element ② of Figure 1. Note that Equations (12) and (13) are now used with

$$2A = (Re)\,u_1^0 \quad \text{and} \quad 2B = (Re)\,u_2^0 \tag{26}$$

where u_1^0 and u_2^0 are now the unknown velocity components at $\mathbf{x} = (0,0)$ in element ②. Thus, Equation (25) is nonlinear, in that the coefficients depend on the velocity field at time $t + \Delta t$. Hence, a fixed point iteration scheme is needed in order to solve (25) at each time step.

The discretization procedure easily generalizes to non-orthogonal curvilinear coordinates, by making use of the mapping procedures described in Section 3 and Appendix B. In such situations, Equations (12) and (13) are used with

$$A = \frac{c_1^0}{\sqrt{g^{11}|_0}} \quad \text{and} \quad B = \frac{c_2^0}{\sqrt{g^{22}|_0}} \tag{27}$$

Copyright © 2005 John Wiley & Sons, Ltd.

where

$$2c_i = Re\,\frac{\partial \xi_i}{\partial x_j}\,u_j - \frac{1}{J}\,\frac{\partial}{\partial \xi_k}(Jg^{ik}) \tag{28}$$

Also, h and k are to be replaced by $1/\sqrt{g^{11}}|_0$ and $1/\sqrt{g^{22}}|_0$ when used in Equations (12) and (13).

Note that the discretization procedure does not invoke the use of a weighted residual statement or minimization statement. It simply makes use of the local analytic interpolant, evaluated at the interior node. A weighted residual statement is not necessary because the interpolant is a local analytic solution to the locally linearized governing equation. Thus, constructing a weighted residual statement may be viewed as redundant since the interpolant satisfies the governing equation locally.

If the pressure field is known *a priori*, then Equation (25) can be written for all global interior nodes, resulting in a banded, definite, un-symmetric system of algebraic equations for the velocity components, which can be solved provided suitable boundary conditions are specified. On a given time step, iterations with respect to the fixed point linearization of Equation (25) are required due to its nonlinear nature. However, in general, the pressure field is unknown, and must be determined such that the velocity field is solenoidal.

4.2. *Pressure–velocity coupling*

The velocity–pressure coupling is achieved by a discrete projection method. The velocity field is first decomposed by projecting out the divergence-free-producing part of the field, i.e. the pressure gradient

$$\mathbf{u} = \hat{\mathbf{u}} + \nabla_h\, p \tag{29}$$

Then, by requesting a solenoidal velocity field, $\nabla^* \cdot \mathbf{u} = 0$, where ∇^* is the discrete divergence operator, we arrive at the following Poisson equation for the pressure:

$$(\nabla^* \cdot \nabla_h)\, p = -\nabla^* \cdot \hat{\mathbf{u}} \tag{30}$$

If velocity is specified at a boundary, then pressure need not be specified there and is computed consistently by extending the projection to that boundary. If velocity is specified on the entire boundary, only a pressure datum need be specified to eliminate the additive pressure constant.

Choosing to retain a co-located degree of freedom arrangement, where the velocity degrees of freedom and pressure degrees of freedom share the same nodal locations, care needs to be exercised in choosing the grid representation of the discrete divergence operator ∇^*. If $\nabla^* = \nabla_h$, then the pressure Poisson equation computational stencil will allow spurious checkerboard-type pressure solutions [1]—which we wish to avoid. Here, we define ∇^* to have a grid representation with a staggered node arrangement to suppress the possibility of spurious pressure solutions. This approach is common practice in finite-difference and control-volume discretizations, when choosing a co-located degree of freedom arrangement [1]. In the following, we present additional details of our implementation, to complement the outline given above.

We consider the general case of a curvilinear non-orthogonal mesh, and work in the space where $\hat{\Omega}_e = [-1, 1] \times [-1, 1]$ such that $\Delta\xi = \Delta\eta = 1.0$ and assume that the mapping $\bar{\Omega}_e \rightleftarrows \hat{\Omega}_e$

Copyright © 2005 John Wiley & Sons, Ltd.

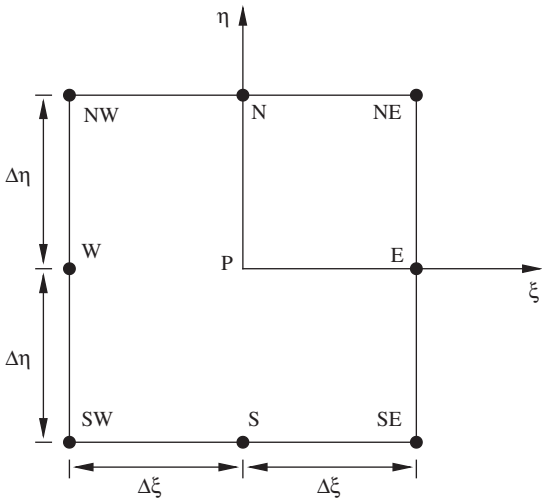

Figure 3. Square element, $\hat{\Omega}_e$, associated with the mapping $\bar{\Omega}_e \rightleftarrows \hat{\Omega}_e$, of dimensions $[-1,1]\times[-1,1]$.

is well defined. Since we will be working with grid difference operators, denoted by δ, we see it convenient to use the compass notation shown in Figure 3, for a typical global interior node P in $\hat{\Omega}_e$.

In view of Equation (25), the decomposition of the velocity field, given by Equation (29), may be written as

$$u_1^{\mathrm{P}} = \hat{u}_1^{\mathrm{P}} - \frac{\alpha_f^{\mathrm{P}}}{1+\alpha_f^{\mathrm{P}}/\Delta t}\left(\frac{\delta p}{\delta x}\right)_{\mathrm{P}}$$

$$u_2^{\mathrm{P}} = \hat{u}_2^{\mathrm{P}} - \frac{\alpha_f^{\mathrm{P}}}{1+\alpha_f^{\mathrm{P}}/\Delta t}\left(\frac{\delta p}{\delta y}\right)_{\mathrm{P}}$$

with

$$\frac{\delta p}{\delta x} = \frac{1}{J}\left(b_1^1\frac{\delta p}{\delta \xi} + b_1^2\frac{\delta p}{\delta \eta}\right)$$

$$\frac{\delta p}{\delta y} = \frac{1}{J}\left(b_2^1\frac{\delta p}{\delta \xi} + b_2^2\frac{\delta p}{\delta \eta}\right)$$

where J is the Jacobian and b_i^l metrics associated with the mapping, $\bar{\Omega}_e \rightleftarrows \hat{\Omega}_e$ (see Appendix B). The decomposition may be written more concisely using indicial notation:

$$u_j^{\mathrm{P}} = \hat{u}_j^{\mathrm{P}} - \left(\frac{\alpha_f}{1+\alpha_f/\Delta t}\frac{b_j^m}{J}\frac{\delta p}{\delta \xi^m}\right)_{\mathrm{P}} \tag{31}$$

Copyright © 2005 John Wiley & Sons, Ltd.

We choose to work with the divergence-free condition in the form

$$\nabla^* \cdot \mathbf{u} = \frac{1}{J} \frac{\delta^*}{\delta \xi^j} (b_i^j u_i) = \frac{1}{J} \frac{\delta^* U^j}{\delta \xi^j} = 0 \tag{32}$$

where $U^i = b_j^i u_i$ are the contravariant velocity components. In view of this choice, the decomposition given in (31) is written in its contravariant form as

$$\begin{aligned} U_{\mathrm{P}}^i &= \hat{U}_{\mathrm{P}}^i - \left(\frac{\alpha_f}{1 + \alpha_f / \Delta t} \frac{b_m^i b_m^j}{J} \frac{\delta p}{\delta \xi^j} \right)_{\mathrm{P}} \\ &= \hat{U}_{\mathrm{P}}^i - E_{\mathrm{P}}^{ij} \left(\frac{\delta p}{\delta \xi^j} \right)_{\mathrm{P}} \end{aligned} \tag{33}$$

The grid representation of the discrete divergence operator, δ^* in (32), is defined at staggered locations to suppress the possibility of spurious pressure solutions. The staggered locations are chosen to lie at $(\xi, \eta) = (\pm 0.5, \pm 0.5)$, from point P in Figure 3. These locations are denoted using lower-case letters in compass notation. Thus, using a second-order approximation in (ξ, η), the discrete divergence-free condition, for a global interior node P, takes the form

$$\left(\frac{\delta^* U^j}{\delta \xi^j} \right)_{\mathrm{P}} = \frac{U_{\mathrm{e}}^1 - U_{\mathrm{w}}^1}{2(\Delta \xi / 2)} + \frac{U_{\mathrm{n}}^2 - U_{\mathrm{s}}^2}{2(\Delta \eta / 2)} = (U_{\mathrm{e}}^1 - U_{\mathrm{w}}^1) + (U_{\mathrm{n}}^2 - U_{\mathrm{s}}^2) = 0 \tag{34}$$

The pressure field that will ensure that the discrete divergence-free condition is satisfied is obtained by substituting (33) into (34), which will give us the Poisson equation for the pressure

$$\frac{\delta^*}{\delta \xi^i} \left(E^{ij} \frac{\delta p}{\delta \xi^j} \right) = \frac{\delta^* \hat{U}^i}{\delta \xi^i} \tag{35}$$

or, equivalently, in semi-discretized form

$$\begin{aligned} &E_{\mathrm{e}}^{11} \left(\frac{\delta p}{\delta \xi} \right)_{\mathrm{e}} + E_{\mathrm{e}}^{12} \left(\frac{\delta p}{\delta \eta} \right)_{\mathrm{e}} - E_{\mathrm{w}}^{11} \left(\frac{\delta p}{\delta \xi} \right)_{\mathrm{w}} - E_{\mathrm{w}}^{12} \left(\frac{\delta p}{\delta \eta} \right)_{\mathrm{w}} + E_{\mathrm{n}}^{22} \left(\frac{\delta p}{\delta \eta} \right)_{\mathrm{n}} + E_{\mathrm{n}}^{21} \left(\frac{\delta p}{\delta \xi} \right)_{\mathrm{n}} \\ &- E_{\mathrm{s}}^{22} \left(\frac{\delta p}{\delta \eta} \right)_{\mathrm{s}} - E_{\mathrm{s}}^{21} \left(\frac{\delta p}{\delta \xi} \right)_{\mathrm{s}} = (\hat{U}_{\mathrm{e}}^1 - \hat{U}_{\mathrm{w}}^1) + (\hat{U}_{\mathrm{n}}^2 - \hat{U}_{\mathrm{s}}^2) \end{aligned} \tag{36}$$

The discrete pressure gradients at the staggered locations are represented using a second-order approximation in (ξ, η). For example, at staggered location e

$$\left(\frac{\delta p}{\delta \xi} \right)_{\mathrm{e}} = \frac{p_{\mathrm{E}} - p_{\mathrm{P}}}{2(\Delta \xi / 2)}$$

$$\left(\frac{\delta p}{\delta \eta} \right)_{\mathrm{e}} = \frac{1}{2} \left(\frac{p_{\mathrm{N}} - p_{\mathrm{S}}}{2 \Delta \eta} + \frac{p_{\mathrm{NE}} - p_{\mathrm{SE}}}{2 \Delta \eta} \right)$$

Copyright © 2005 John Wiley & Sons, Ltd.

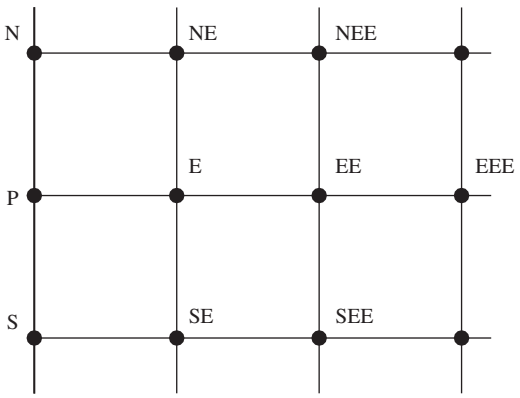

Figure 4. Computational stencil near a boundary in (ξ, η) space.

and similarly for other staggered locations. In this manner, we arrive at the fully discretized Poisson equation for the pressure, resulting in a stencil relating nine contiguous nodal pressure degrees of freedom:

$$\beta^0 p^0 - \sum_{n=1}^{8} \beta_n \, p_n = -\hat{D}^0 \tag{37}$$

where the nodes are numbered as shown in Figure 1, with the location of the interior node being denoted by the superscript '0'. The coefficients $\{\beta_n\}_{n=1}^{8}$, β^0 are defined as follows:

$$\begin{aligned}
\beta_1 &= \tfrac{1}{4}(E_{\mathrm{w}}^{12} + E_{\mathrm{s}}^{21}), & \beta_5 &= E_{\mathrm{s}}^{22} - \tfrac{1}{4}(E_{\mathrm{e}}^{12} - E_{\mathrm{w}}^{12}) \\
\beta_2 &= -\tfrac{1}{4}(E_{\mathrm{e}}^{12} + E_{\mathrm{s}}^{21}), & \beta_6 &= E_{\mathrm{e}}^{11} - \tfrac{1}{4}(E_{\mathrm{s}}^{21} - E_{\mathrm{n}}^{21}) \\
\beta_3 &= \tfrac{1}{4}(E_{\mathrm{e}}^{12} + E_{\mathrm{n}}^{21}), & \beta_7 &= E_{\mathrm{n}}^{22} - \tfrac{1}{4}(E_{\mathrm{w}}^{12} - E_{\mathrm{e}}^{12}) \\
\beta_4 &= -\tfrac{1}{4}(E_{\mathrm{w}}^{12} + E_{\mathrm{n}}^{21}), & \beta_8 &= E_{\mathrm{w}}^{11} - \tfrac{1}{4}(E_{\mathrm{n}}^{21} - E_{\mathrm{s}}^{21})
\end{aligned} \tag{38}$$

$$\beta^0 = \sum_{n=1}^{8} \beta_n = E_{\mathrm{e}}^{11} + E_{\mathrm{w}}^{11} + E_{\mathrm{n}}^{22} + E_{\mathrm{s}}^{22} \tag{39}$$

with

$$\hat{D}^0 = (\hat{U}_{\mathrm{e}}^1 - \hat{U}_{\mathrm{w}}^1) + (\hat{U}_{\mathrm{n}}^2 - \hat{U}_{\mathrm{s}}^2) \tag{40}$$

Equation (37) can be written for all global interior nodes, resulting in a banded, definite, un-symmetric system of algebraic equations for the pressure, which can be solved provided suitable boundary conditions are specified. If the mesh is orthogonal, $E^{12} = E^{21} = 0$, the system of algebraic equations will have a symmetric structure.

If velocity is specified at a boundary, then pressure need not be specified there and is computed consistently by applying the projection at all nodes that lie on that boundary. For example, consider the boundary node P shown in Figure 4. Using a second-order

Copyright © 2005 John Wiley & Sons, Ltd.

approximation in (ξ, η), the discrete divergence-free condition, for the boundary node P, takes the form

$$\left(\frac{\delta^* U^j}{\delta \xi^j}\right)_{\mathrm{P}} = \frac{-U^1_{\mathrm{EE}} + 4U^1_{\mathrm{E}} - 3\bar{U}^1_{\mathrm{P}}}{2\Delta\xi} + \frac{\bar{U}^2_{\mathrm{N}} - \bar{U}^2_{\mathrm{S}}}{2\Delta\eta} = 0 \tag{41}$$

where the overbar implies that those velocity components are specified. Note that the grid representation of the discrete divergence at the boundary was written in terms of node locations, and *not* in terms of staggered locations, as is necessary for interior nodes—to avoid decoupled networks of pressure degrees of freedom that may excite spurious pressure solutions. This is not a danger at the boundary, due to the one-sided grid representation.

Applying decomposition (33) to the velocities at node E and EE, and substituting into (41), yields a pressure equation for the boundary node P of Figure 4.

$$E^{11}_{\mathrm{E}}\, p_{\mathrm{P}} = E^{11}_{\mathrm{E}}\, p_{\mathrm{EE}} - \frac{1}{4} E^{11}_{\mathrm{EE}}(p_{\mathrm{EEE}} - p_{\mathrm{E}}) + E^{12}_{\mathrm{E}}(p_{\mathrm{NE}} - p_{\mathrm{SE}})$$
$$-\frac{1}{4} E^{12}_{\mathrm{EE}}(p_{\mathrm{NEE}} - p_{\mathrm{SEE}}) - \left(\frac{-\hat{U}^1_{\mathrm{EE}} + 4\hat{U}^1_{\mathrm{E}} - 3\bar{U}^1_{\mathrm{P}}}{2} + \frac{\bar{U}^2_{\mathrm{N}} - \bar{U}^2_{\mathrm{S}}}{2}\right)$$

Such equation, is written for all boundary nodes that lie on that boundary. Similar expressions are easily derived for nodes on other boundaries.

If velocity is specified on the entire boundary Γ^h, then the projection is applied at all the boundary nodes. In this case, one need only specify pressure at a single node (i.e. a datum), and the resulting discrete set of algebraic equations will be a Gramm matrix, needing no additional boundary conditions to be invertible.

4.3. Solution strategy

In our work we adopt a sequential solution procedure, where the discretized momentum equations (25) are solved first, using the latest pressure field. Then, the Poisson equation for the pressure (37) is solved, using the latest velocity field. Upon obtaining the pressure field, the velocity field is made solenoidal by projecting it onto a div-free space via Equation (31). Step-by-step details on the solution strategy are given in the following.

Given an initial condition for the velocity field and an initial guess for the pressure field, the following steps are followed to time-advance the velocity and pressure fields such that the incompressible Navier–Stokes equations are satisfied at each time step

1. Compute the finite analytic coefficients, $\{\alpha^0_n\}^8_{n=1}$, α^0_f, at all interior global nodes using the latest velocity field.
2. Construct and solve the set of algebraic equations associated with the discretized momentum equations (25). Use the latest pressure field to evaluate the pressure gradient on the right-hand side of (25), i.e. treat the pressure field explicitly.
3. Project the resulting velocity field onto a div-free space as follows:
   - Compute the coefficients associated with the discrete Poisson equation for the pressure, $\{\beta_n\}^8_{n=1}$, β^0, at all interior global nodes.

Copyright © 2005 John Wiley & Sons, Ltd.

- Construct and solve the set of algebraic equations associated with the Poisson equation for the pressure (37). Use the latest velocity field to evaluate the right-hand side of (37), i.e. treat the velocity field explicitly.
- Make the velocity field solenoidal by adding back the pressure gradient, using Equation (31).

4. Repeat the projection step (3), until the initial divergence of the velocity field drops by one or two orders of magnitude. This is typically achieved in at most two projection steps.
5. Repeat steps (1–4) to account for the fixed point linearization of Equation (25), i.e. to account for the nonlinearity associated with the momentum equations.
   - At this point, under-relaxation of the pressure field may be necessary in order to allow the velocity field in step (2) to respond smoothly to the pressure gradient that causes it to be solenoidal. Typically, under-relaxation is only needed if the time-step size is large or the transients of the problem are significant.
   - If the time step is small, then the finite analytic coefficients in step (1) need not be re-evaluated. This essentially amounts to linearizing the momentum equation about the previous time step. In such an approach, iterations at this level are still needed if pressure is under-relaxed. Instead of 'nonlinear iterations', these iterations receive the name of 'outer iterations'—although sometimes these names are used interchangeably.
   - Do not time-advance the velocity and pressure fields until a tolerance criteria between successive nonlinear/outer iterations is met. The recommended convergence measure is the L_1 norm of the momentum residuals [1], as the normalized difference between successive nonlinear/outer iterations may be misleading if under-relaxation is used.
   - If time accuracy is not desired, e.g. marching fast towards a steady-state, then time-advance the velocity and pressure fields immediately after step (4). In such cases, we adopt the terminology: 'iterating towards a steady-state', rather than 'time stepping to a steady-state' because time accuracy is not enforced.
6. Repeat steps (1–5) until the desired time level is reached or a steady-state is achieved.

On a given time step and nonlinear/outer iteration, the system of equations associated with the velocity components are solved iteratively using a line-by-line tri-diagonal alternating-direction-implicit (ADI) algorithm. Iterations are stopped when the initial residual drops by one or two orders of magnitude, typically achieved in 3–5 ADI iterations. In turn, the system of equations associated with the pressure is solved iteratively using Stone's strongly implicit procedure [16] (SIP)—which gives superior convergence rates when compared to an ADI algorithm for the same equation (see Section 5.1). Iterations are stopped when the initial residual drops by one or two orders of magnitude, typically achieved in 5–10 SIP iterations.

4.4. Extension to the three-dimensional case

In three-dimensions, a local analytic solution is readily obtained in a rectangular three-dimensional element by the method of separation of variables. The procedure is a straightforward extension of that presented in Appendix A, for the two-dimensional case, and is documented in Reference [12]. The resulting coefficients are used to construct a stencil relating 27 nodal variables and require the evaluation of three infinite series.

In our work, we construct a computationally less-demanding set of coefficients, by superimposing sets of two-dimensional coefficients in such manner that the three-dimensional

Copyright © 2005 John Wiley & Sons, Ltd.

governing equation is satisfied. To illustrate, consider the three-dimensional form of Equation (7),

$$u_1 \frac{\partial \theta}{\partial x} + u_2 \frac{\partial \theta}{\partial y} + u_3 \frac{\partial \theta}{\partial z} - \frac{1}{Pe}\left(\frac{\partial^2 \theta}{\partial x^2} + \frac{\partial^2 \theta}{\partial y^2} + \frac{\partial^2 \theta}{\partial z^2}\right) = f \tag{42}$$

which may be written in any of the following three alternate forms:

$$u_2 \frac{\partial \theta}{\partial y} + u_3 \frac{\partial \theta}{\partial z} - \frac{1}{Pe}\left(\frac{\partial^2 \theta}{\partial y^2} + \frac{\partial^2 \theta}{\partial z^2}\right) = g_x, \quad g_x = f - u_1 \frac{\partial \theta}{\partial x} + \frac{1}{Pe}\frac{\partial^2 \theta}{\partial x^2} \tag{43}$$

$$u_1 \frac{\partial \theta}{\partial x} + u_3 \frac{\partial \theta}{\partial z} - \frac{1}{Pe}\left(\frac{\partial^2 \theta}{\partial x^2} + \frac{\partial^2 \theta}{\partial z^2}\right) = g_y, \quad g_y = f - u_2 \frac{\partial \theta}{\partial y} + \frac{1}{Pe}\frac{\partial^2 \theta}{\partial y^2} \tag{44}$$

$$u_1 \frac{\partial \theta}{\partial x} + u_2 \frac{\partial \theta}{\partial y} - \frac{1}{Pe}\left(\frac{\partial^2 \theta}{\partial x^2} + \frac{\partial^2 \theta}{\partial y^2}\right) = g_z, \quad g_z = f - u_3 \frac{\partial \theta}{\partial z} + \frac{1}{Pe}\frac{\partial^2 \theta}{\partial z^2} \tag{45}$$

Regarding each of the above as two-dimensional equations in constant x-, y- and z-planes, we construct for each of them a two-dimensional local analytic interpolant, as described in Section 3. When the interpolant is evaluated at an interior node, located at $\mathbf{x} = (0, 0, 0)$, the following set of expressions result:

$$\theta(\mathbf{0}) = \sum_{n=1}^{8} \alpha_n^{0,x} \theta_n^x - \alpha_f^{0,x} g_x \tag{46}$$

$$\theta(\mathbf{0}) = \sum_{n=1}^{8} \alpha_n^{0,y} \theta_n^y - \alpha_f^{0,y} g_y \tag{47}$$

$$\theta(\mathbf{0}) = \sum_{n=1}^{8} \alpha_n^{0,z} \theta_n^z - \alpha_f^{0,z} g_z \tag{48}$$

In view of Equation (42), which is equivalent to requiring $-g_x - g_y - g_z + 2f = 0$, we arrive at the three-dimensional discretization of (42),

$$\theta(\mathbf{0}) = \theta^0 = \frac{\sum_{n=1}^{8} \alpha_n^{0,x} \theta_n^x + \sum_{n=1}^{8} \alpha_n^{0,y} \theta_n^y + \sum_{n=1}^{8} \alpha_n^{0,z} \theta_n^z - 2f}{1/\alpha_f^{0,x} + 1/\alpha_f^{0,y} + 1/\alpha_f^{0,z}} \tag{49}$$

from which a stencil relating 19 nodal variables is extracted. The three-dimensional finite analytic coefficients, $\{\alpha_n^{0,3\text{-D}}\}_{n=1}^{18}$, $\alpha_f^{0,3\text{-D}}$, are but a superposition of two-dimensional finite analytic coefficients according to Equation (49). Additional details may be found in Reference [17], where this approach first appeared. Yet another possibility, is a stencil relating 11 nodal variables, proposed in Reference [18], for flows with a predominant flow direction.

In non-orthogonal curvilinear coordinates the above procedure applies, but the decomposition is made in ξ-, η- and ζ-constant planes. The three-dimensional numerical results presented in Section 5.6, use the above discretization procedure.

Copyright © 2005 John Wiley & Sons, Ltd.

5. NUMERICAL EXAMPLES

5.1. Kovasznay flow

A first benchmark problem to be used for the purposes of verification is an analytic solution to the two-dimensional, stationary incompressible Navier–Stokes due to Kovasznay [19]. The spatial domain in which Kovasznay's solution is defined is taken here as the bi-unit square $\bar{\Omega} = [-0.5, 1.5] \times [-0.5, 1.5]$. The solution is given by

$$\begin{aligned} u(x, y) &= 1 - \mathrm{e}^{\lambda x} \cos(2\pi y) \\ v(x, y) &= \frac{\lambda}{2\pi} \mathrm{e}^{\lambda x} \sin(2\pi y) \\ p(x, y) &= p_0 - \tfrac{1}{2} \mathrm{e}^{2\lambda x} \end{aligned} \tag{50}$$

where $\lambda = Re/2 - (Re^2/4 + 4\pi^2)^{1/2}$, p_0 is a reference pressure (an arbitrary constant), and we choose $Re = 40$.

Here, we perform a h-refinement study and expect the error measures to decay at an algebraic rate as the mesh is refined. In a log–log scale the expected rate of convergence would appear as a straight line. The error measures are taken here to be the r.m.s. L_2 norms of the difference between the numerical solution and the analytic solution. Convergence of this measure to zero implies that the numerical solution approaches the exact solution.

The discretization procedures do not lend themselves to a rigorous *a priori* error estimation analysis, as they are not based on Taylor expansions (like finite differences) or variational statements (like finite elements). Nevertheless, we expect the discretization to be at least second-order accurate because it satisfies zeroth- and first-order consistency requirements.

5.1.1. Test 1. In this first numerical test we wish to establish the order of consistency of the interpolants. This is achieved by making the pressure gradient and velocity fields analytically available at all nodes for the purpose of evaluating an *interpolated* velocity field at all interior global nodes via Equation (11). This exercise is repeated in successively refined meshes, starting from 21×21 up to 161×161 uniformly spaced nodes in $\bar{\Omega}^h$.

In Figure 5(a) we plot the r.m.s. L_2 error of the velocity field for successively refined meshes in a log–log scale. We see that an algebraic convergence rate of $\mathcal{O}(h^4)$ is achieved. This indicates the existence of higher-order consistency in the interpolants.

5.1.2. Test 2. In this and subsequent tests, we establish the asymptotic rate of convergence of the local-analytic-based discretization procedure in various relevant scenarios. Here, we use the exact solution, given by Equation (50), to prescribe Dirichlet velocity boundary conditions on Γ^h. In addition, we make the pressure gradient analytically available at all global interior nodes and we make the problem linear by making the velocity field analytically available *only* to evaluate the finite analytic coefficients at all global interior nodes. In essence, we are solving a linear advection–diffusion problem, where the convective velocity field and source term are prescribed.

Five different uniform meshes are used to perform the h-refinement study. The meshes are successively refined starting from 21×21 to 321×321 uniformly spaced nodes in $\bar{\Omega}^h$.

Copyright © 2005 John Wiley & Sons, Ltd.

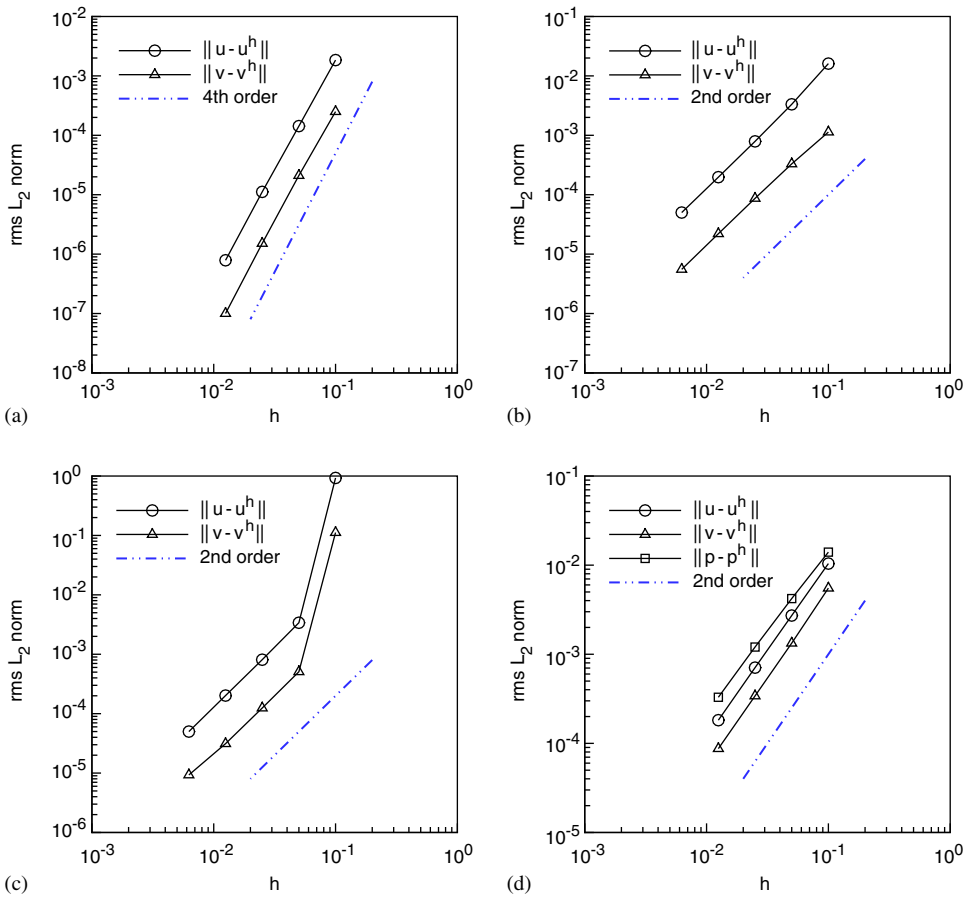

Figure 5. *h*-convergence of error measures to the Kovasznay solution in the r.m.s. L_2 norm: (a) interpolation error of the velocity field; (b) discretization error of the velocity field for a linear equation model; (c) discretization error of the velocity field for a nonlinear equation model; and (d) discretization error of the velocity and pressure fields for the incompressible Navier–Stokes equations.

In Figure 5(b) we plot the r.m.s. L_2 error of the velocity field for successively refined meshes in a log–log scale. We see that an algebraic convergence rate of $\mathcal{O}(h^2)$ is achieved for the discretization procedure. The deterioration in the rate of convergence, from potentially $\mathcal{O}(h^4)$ to $\mathcal{O}(h^2)$, is inherent to the discretization procedure; which only collocates at the centre of the element.

5.1.3. Test 3. In this next numerical test, Dirichlet velocity boundary conditions are prescribed on Γ^h and the pressure gradient is analytically available at all global interior nodes. This time we are solving a nonlinear advection–diffusion problem with a prescribed source term (i.e. the momentum equations with a prescribed pressure gradient field).

In Figure 5(c) we plot the r.m.s. L_2 error of the velocity field for successively refined meshes in a log–log scale. In the coarsest mesh the error due to linearization is large, but

Copyright © 2005 John Wiley & Sons, Ltd.

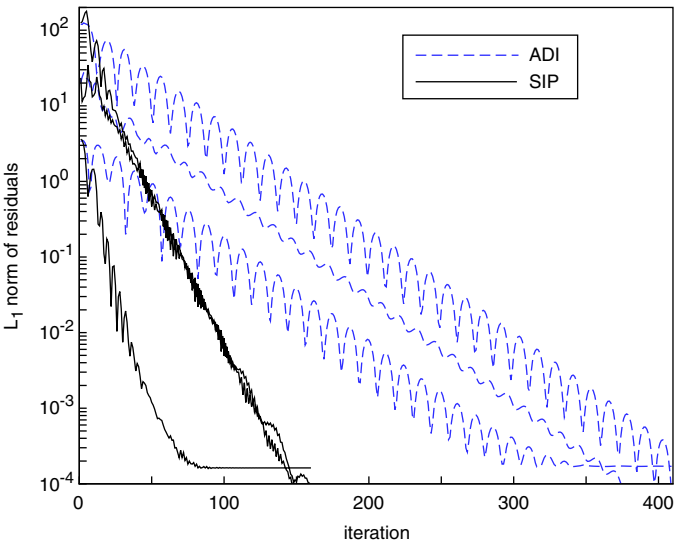

Figure 6. Convergence history, showing decay of the L_1 norm of momentum residuals and L_1 norm of the dilatation. Comparison when ADI and SIP solvers are used for the pressure Poisson equation.

reduces quickly as the mesh is refined; with error values nearly identical to the linear case. We see that the spatial linearization of the convective term does not impact the convergence rate of the discretization procedure, which remains as $\mathcal{O}(h^2)$. Higher-order spatial linearizations of the convective terms, e.g. a weighted average of neighbouring values, have negligible effects and do not improve the asymptotic convergence rate. Thus, the simple centre-valued spatial linearization is retained.

5.1.4. Test 4. In this last test, we solve the incompressible Navier–Stokes equations. Dirichlet velocity boundary conditions are prescribed on Γ^h and pressure is specified at a point. The velocity field on the interior of the domain is to be computed and the pressure field is to be computed in *all* the domain, including at the boundaries.

In Figure 5(d) we plot the r.m.s. L_2 error of the velocity and pressure fields for successively refined meshes in a log–log scale. We see that an algebraic convergence rate of $\mathcal{O}(h^2)$ is achieved for velocities and pressure. The convergence rate of $\mathcal{O}(h^2)$ is retained for the velocities and the same rate is achieved for the pressure, indicating good velocity–pressure coupling by the segregated solution strategy.

Figure 6 shows the convergence history for the simulation in the 161×161 uniform mesh. The error measures shown are the L_1 norm of momentum residuals and L_1 norm of the dilatation. Iterations are stopped when the maximum L_1 residual of either momentum equations falls below 10^{-4}. In Figure 6 we demonstrate the improvement in convergence rate that is achieved when the Poisson equation for the pressure is solved using the SIP procedure, as opposed to the line-by-line ADI procedure. By using the SIP solver, we see that the number of iterations required to meet the convergence criteria is reduced by a factor of two or better. We emphasize that both simulations use the line-by-line ADI solver for the momentum equations.

Copyright © 2005 John Wiley & Sons, Ltd.

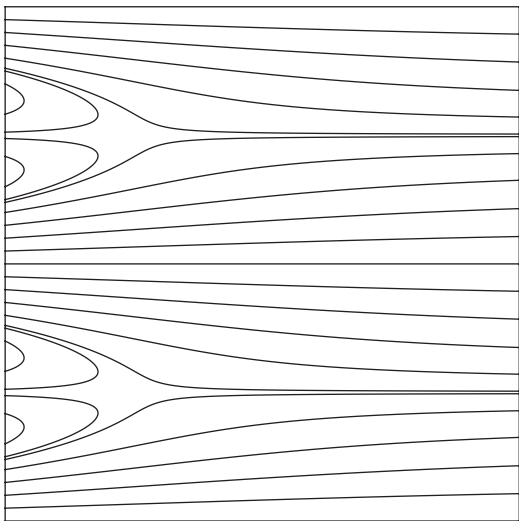

Figure 7. Computed streamlines showing the pattern of the Kovasznay flow.

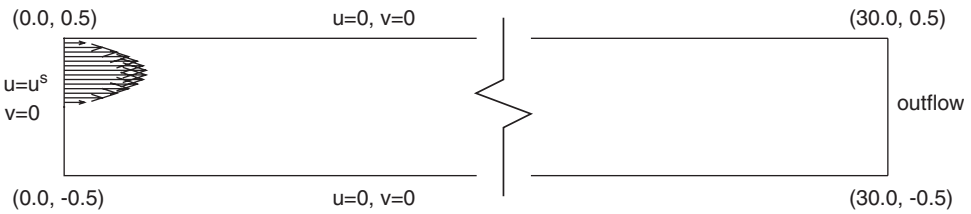

Figure 8. Geometry and boundary conditions for flow over a backward-facing step.

With this in mind, it is interesting to see the strong effect the decay of the dilatation has on the overall convergence of the solution procedure.

Yet another important detail from Figure 6, is that the value of the L_1 norm of the dilatation saturates slightly above 10^{-4}. This is a well-known side-effect of having chosen the grid representation of the discrete divergence to be defined at staggered locations—to prevent spurious pressure solutions. The value at which the dilatation saturates is proportional to the grid size squared, the time-step size, and the local value of the fourth derivative of the pressure [20]. Approaches exist to lower the saturation level of the dilatation [20], but are not implemented in this study.

The computed streamlines using the 161×161 mesh are shown in Figure 7. As noted in the original work of Kovasznay [19], the flow resembles laminar low-speed flow behind an array of bluff bodies.

5.2. *Flow over a backward-facing step*

We consider the two-dimensional flow over a backward-facing step at $Re = 800$. The geometry and boundary conditions are taken from the benchmark solution of Gartling [21] and are shown in Figure 8. As shown in Figure 8 the standard step geometry was simplified by

Copyright © 2005 John Wiley & Sons, Ltd.

Table I. Comparison of computed separation/reattachment points for flow over a backward-facing step at $Re = 800$ for increasing spatial resolution.

	x_1^{rea}	x_2^{sep}	x_2^{rea}
301×41 uniform	5.00	4.00	10.00
601×81 uniform	5.65	4.55	10.15
801×81 non-uniform	6.05	4.80	10.40
Gartling [21]	6.10	4.85	10.50

excluding the channel portion upstream of the step. The boundary conditions for the step geometry include the no-slip condition at all solid surfaces and a parabolic inlet velocity profile given by $u(y) = 24y(0.5 - y)$ for $0 \leqslant y \leqslant 0.5$. The outflow boundary conditions is of the form $-p + (1/Re)\partial u/\partial x = 0$, $\partial v/\partial x = 0$. The Reynolds number is based on the mean inlet velocity and the channel height.

Initially, we discretize the domain, $\bar{\Omega} = [0, 30] \times [-0.5, 0.5]$, using two successively finer uniform meshes: a 301×41 node mesh followed by a 601×81 node mesh. The 301×41 grid gives a uniform spacing of $\Delta x = 0.10, \Delta y = 0.025$, and the 601×81 grid a uniform spacing of $\Delta x = 0.05$, $\Delta y = 0.0125$.

The flow separates at the step corner and forms a large recirculation region with a reattachment point on the lower wall of the channel at $x = 6.10$ [21]. A second recirculation region forms on the upper wall of the channel beginning at $x = 4.85$ with a reattachment point at $x = 10.50$ [21]. Table I shows the predicted separation/reattachment points on the two successively finer meshes. We see that we are still far from the target values, taken here to be those reported in the benchmark solution of Gartling [21], who used a 600×30 finite element mesh with bi-quadratic approximation for velocities and discontinuous linear approximation for the pressure, i.e. 73 261 velocity nodes and 54 000 pressure stations.

To improve the solution we design a non-uniform 801×81 node mesh, with uniform spacing $\Delta y = 0.0125$ throughout. In the upstream region $0 \leqslant x \leqslant 15$ the grid points are uniformly spaced with $\Delta x = 0.025$. For the region $15 \leqslant x \leqslant 30$ the grid point distribution is smoothly graded from $\Delta x = 0.025$ to $\Delta x = 0.075$. Table I shows the improvement of the predicted flow metrics. Figure 9 shows the computed streamlines on the three successively finer meshes, for $0 \leqslant x \leqslant 12$, where most of the interesting flow structures occur.

In Figure 10 we plot the computed pressure profiles along the length of the channel's lower wall. For comparison, we include the profile reported in Reference [9], computed using a spectral/*hp* least-squares finite element formulation—using a 10×2 uniform mesh with expansion orders of 11 in each element and in each direction. We see good agreement, especially for the finer meshes. Note that the slopes of the pressure profiles become constant near the exit plane, meaning that the flow has recovered to fully developed conditions at the exit. Figure 11 shows computed u-velocity profiles along the channel height at $x = 7$. We compare with tabulated values from the benchmark solution of Gartling [21] and find good agreement.

5.3. *Lid-driven flows in skewed cavities*

So far, we have only presented numerical examples where the grid lines are orthogonal to each other, i.e. orthogonal grids. In practice, we will seldom encounter such well-behaved grids.

Copyright © 2005 John Wiley & Sons, Ltd.

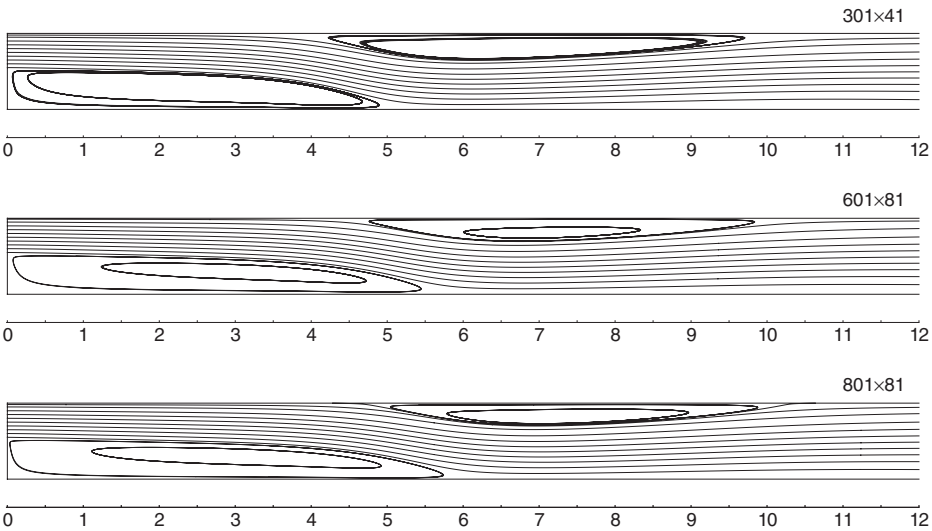

Figure 9. Computed streamlines on three different grids. As the mesh is refined, the separation/reattachment points tend towards their 'mesh-independent locations'.

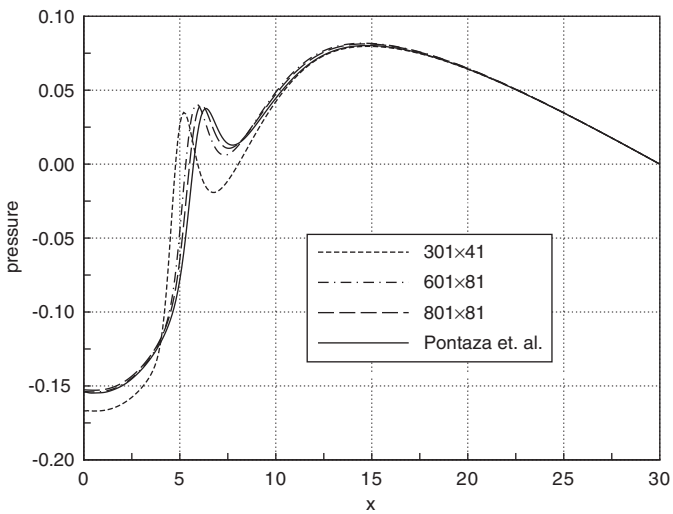

Figure 10. Computed pressure along the lower wall of the channel for the three different meshes. Comparison with the pressure profile reported in Reference [9] using a spectral/*hp* least-squares finite element formulation.

Typically, when considering flow around complex geometries, the grid will have regions with mild non-orthogonality and other regions with strong non-orthogonality. It is thus relevant to study the behaviour of the formulation when used in non-orthogonal grids, and thus establish whether or not it is able to handle mild and strong mesh skews.

Copyright © 2005 John Wiley & Sons, Ltd.

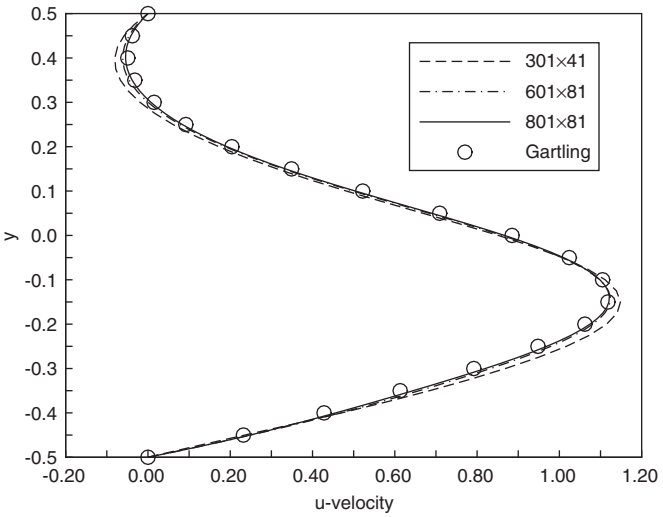

Figure 11. Computed u-velocity profiles along the channel height at $x = 7$. Comparison with tabulated data of Gartling [21].

To this end, we consider the numerical solution of lid-driven flows in skewed cavities, and construct the mesh by using grid lines that are parallel to the walls—thus creating the desired non-orthogonality. First we consider a cavity with skew angle $\beta = 45°$, which may be viewed as a mild case of non-orthogonality. Then, we consider a strong case of non-orthogonality, using a cavity with skew angle $\beta = 30°$. In practice, it is customary to aim towards a well-behaved mesh, so that we will seldom see a skew angle of 30°. Nevertheless, it is important to consider these extreme cases to build confidence in the formulation.

5.3.1. Simulations at skew angle $\beta = 45°$. We consider flow conditions of $Re = 1000$ and grids with uniform node distributions of 41×41, 81×81, and 161×161. Two velocity projections onto div-free space were made per outer iteration, this practice was observed to accelerate convergence significantly in non-orthogonal grids. Outer iterations were stopped when the L_1 norm of the momentum residuals was less that 10^{-3}. The simulation on the 41×41 grid was started from zero initial fields, simulations on subsequent grids were started by interpolating the solution from the coarser grid onto the finer one.

Figure 12 shows the computed u-velocity profiles along the cavity's skewed centreline. We see good agreement with the benchmark solution of Demirdzic *et al.* [22], reported for a 320×320 control-volume mesh using central differences to approximate both convection and diffusive fluxes and a multigrid solution procedure. Figure 13 shows computed streamlines and pressure contours in the skewed cavity for the 161×161 grid.

5.3.2. Simulations at skew angle $\beta = 30°$. As before, we consider flow conditions of $Re = 1000$ and grids with uniform node distributions of 41×41, 81×81, and 161×161. Figure 14 shows the computed u-velocity profiles along the cavity's skewed centreline. We see good

Copyright © 2005 John Wiley & Sons, Ltd.

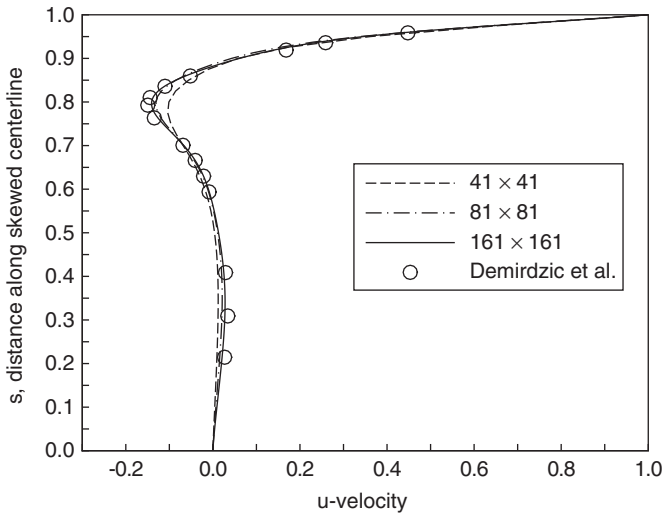

Figure 12. Computed u-velocity profiles along the cavity's 45° skewed centreline. Comparison with tabulated data of Demirdzic *et al.* [22].

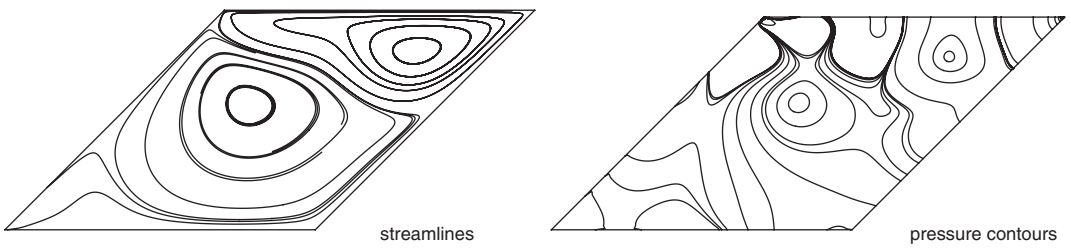

Figure 13. Computed streamlines and pressure contours in the 45° skewed cavity at flow conditions of $Re = 1000$. 161×161 uniform grid.

agreement with the benchmark solution of Demirdzic *et al.* [22]. Figure 15 shows computed streamlines and pressure contours in the skewed cavity for the 161×161 grid.

5.4. Oscillatory lid-driven cavity flow

We now turn attention to the time accurate numerical solution of incompressible fluid flows, and consider flow inside a square cavity driven by an oscillatory lid. The fluid is initially in a steady-state motion brought about by the translation of the top boundary. The top boundary suddenly begins to oscillate in a periodic fashion, according to the cosine distribution: $u_{\text{lid}}(t) = \cos(t)$, with period $\mathscr{T} = 2\pi$.

The Reynolds number considered here is 400, and we use a 81×81 uniform grid on $\bar{\Omega} = [0, 1] \times [0, 1]$. The temporal terms are discretized by a backward Euler representation. For the time marching procedure the size of the time step was chosen as $\Delta t = 0.05$; so that

Copyright © 2005 John Wiley & Sons, Ltd.

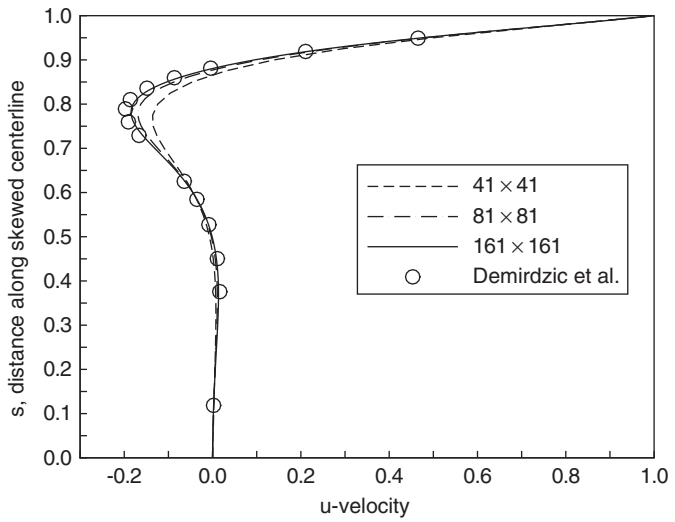

Figure 14. Computed u-velocity profiles along the cavity's 30° skewed centreline. Comparison with tabulated data of Demirdzic *et al.* [22].

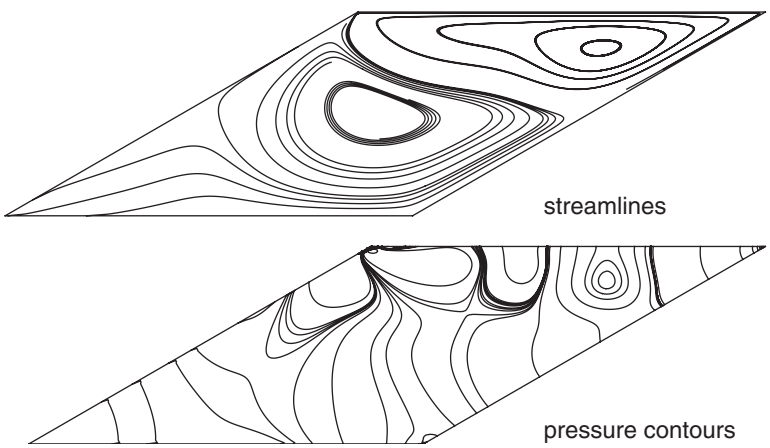

Figure 15. Computed streamlines and pressure contours in the 30° skewed cavity at flow conditions of $Re = 1000$. 161×161 uniform grid.

approximately 125 time steps make one period. We march in time until a periodic steady-state is well established.

Figure 16 shows the time history up to $t = 100.0 \approx 16\mathscr{T}$ of the u-velocity component at two locations along the vertical mid-line of the cavity, one 0.2 units away from the lid and the other 0.2 units away from the bottom surface. Also shown are time history results reported by Pontaza and Reddy [10], for the same problem and flow conditions, using a space–time coupled spectral/hp least-squares finite element formulation with expansions of order 5 in

Copyright © 2005 John Wiley & Sons, Ltd.

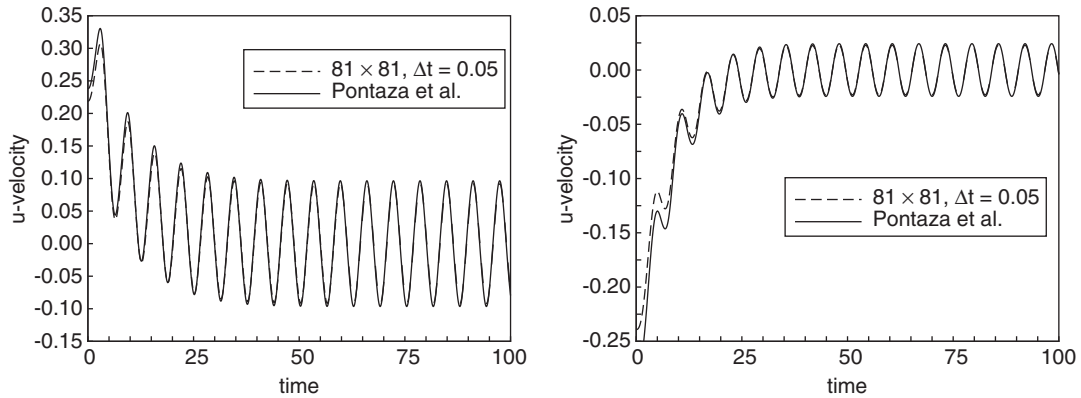

Figure 16. Time history of the *u*-velocity component at two selected locations along the vertical mid-line of the cavity. Comparison with the time history reported by Pontaza and Reddy [10], using a space–time coupled spectral/*hp* least-squares finite element formulation.

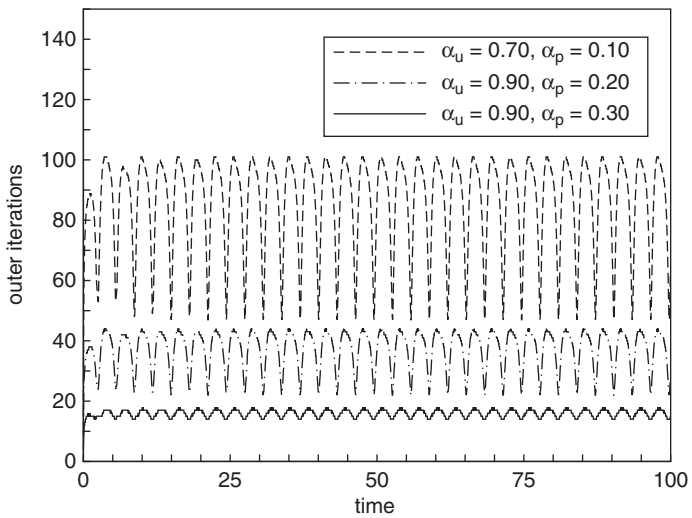

Figure 17. Number of outer iterations required per time step to achieve an L_1 residual tolerance of 10^{-3} for three different choices of relaxation factors.

space and expansions of order 2 in time. We see excellent agreement, implying good time accurate results by the formulation.

Also of relevance is the cost of the time accurate simulation. Figure 17 shows the number of outer iterations required per time step to achieve an L_1 residual tolerance of 10^{-3} for three different choices of relaxation factors for velocities and pressure. By going from $\alpha_u = 0.70, \alpha_p = 0.10$ to $\alpha_u = 0.90, \alpha_p = 0.30$, the simulation is sped-up by nearly a factor of 10. No significant speed-up was further obtained by increasing the relaxation factors, e.g. at $\alpha_u = 1.00, \alpha_p = 0.50$ no appreciable decrease in the number of outer iterations per time step required to achieve the prescribed tolerance was observed—although the simulation remained perfectly stable at such values of α_u, α_p.

Copyright © 2005 John Wiley & Sons, Ltd.

Such a stringent L_1 residual tolerance is not necessary to obtain a time accurate response, and was used here simply to illustrate the sensitivity of the formulation to the relaxation factors. Thus, for high accuracy at minimum cost, $0.90 \leqslant \alpha_u \leqslant 1.00$, $0.30 \leqslant \alpha_p \leqslant 1.00$ is desirable.

5.5. *Unsteady flow past a circular cylinder*

We consider the two-dimensional flow of an incompressible fluid past a circular cylinder. At low Reynolds numbers ($5 < Re < 40$) the flow is stationary and characterized by a pair of standing vortices appearing behind the cylinder. The size of the separated flow region increases with increasing Reynolds number, until a limit in which the wake becomes unstable. At this critical Reynolds number, $Re_c \approx 46.2$ [23, 24], vortices are shed from the aft of the circular cylinder, forming the well-known von Karman vortex street. The flow may be treated as two-dimensional until $Re_c^{3\text{-D}} \approx 188.5$ [25], at which point the cylinder wake becomes three-dimensional due to a secondary instability of the vortex street.

We wish to demonstrate the predictive capabilities of the formulation for a wide range of Reynolds numbers, and especially at high Reynolds numbers. To this end we perform a set of simulations spanning the Reynolds number range $\mathcal{O}(10^1)$–$\mathcal{O}(10^7)$ which covers sub-, trans-, super- and post-critical flow regimes for separated flows around bluff bodies. In spite of the fact that the flow is no longer two-dimensional above $Re_c^{3\text{-D}} \approx 188.5$, we expect the simulation results to qualitatively follow experimentally observed behaviour. The Reynolds number is based on the free-stream velocity, U_∞, and the cylinder diameter, D.

The boundary conditions are as follows: free-stream conditions $u = U_\infty = 1.0$, $v = 0$ at the inflow, far-field no flux conditions $\partial u/\partial y = 0$, $v = 0$ at the lateral boundaries, no-slip conditions $u = v = 0$ on the cylinder surface, and outflow boundary conditions of the form $-p + (1/Re)\,\partial u/\partial x = 0$, $\partial v/\partial x = 0$.

The computational domain is an overset (Chimera) grid, consisting of four overlapping and embedded grid systems. The first grid, $\bar{\Omega}_1^h = [-15.5, 20.5] \times [-15.5, 15.5]$, is a background mesh with uniform spacing $\Delta x = \Delta y = 0.25$. The second grid, $\bar{\Omega}_2^h = [-3.0, 10.0] \times [-3.0, 3.0]$, is embedded in $\bar{\Omega}_1^h$ and is a mesh with uniform spacing $\Delta x = \Delta y = 0.10$ for the purpose of resolving the far-wake flow field. The third grid, $\bar{\Omega}_3^h = [-2.0, 3.0] \times [-2.0, 2.0]$, is embedded in $\bar{\Omega}_2^h$ and is a mesh with uniform spacing $\Delta x = \Delta y = 0.05$ for the purpose of resolving the near-wake flow field immediately behind the circular cylinder. The fourth grid, $\bar{\Omega}_4^h$, is a cylindrical mesh centred at $(0, 0)$ with inner radius 0.5 and outer radius 1.0, and is embedded in the Cartesian grids.

Simulations are performed for increasingly finer cylindrical grids with sizes $(N_r \times N_\theta)$ as follows: M1 (51×181), M2 (61×361), M3 (121×361), and M4 (131×721). The Cartesian near-wake grid, on which the cylindrical grid is embedded, is refined consistently as well. The zonal-based resolution is one of the advantages of overset grids, allowing refinement of the near-wake grids independent from the surrounding Cartesian grids.

The nodes in the circumferential direction are equi-spaced and the node distribution in the radial direction maintains a near-wall spacing of 5×10^{-7}, to adequately resolve viscous near-wall effects. Thus, we consider cell aspect ratios in the near-wall region of the order $1{:}10^5$. We find that the formulation is insensitive to such high cell aspect ratios, further attesting to its robustness.

The overset grid with M1 resolution is shown in Figure 18. The *hole cutting* and *donor search* procedures are not described here and the interested reader is referred to Reference [26],

Copyright © 2005 John Wiley & Sons, Ltd.

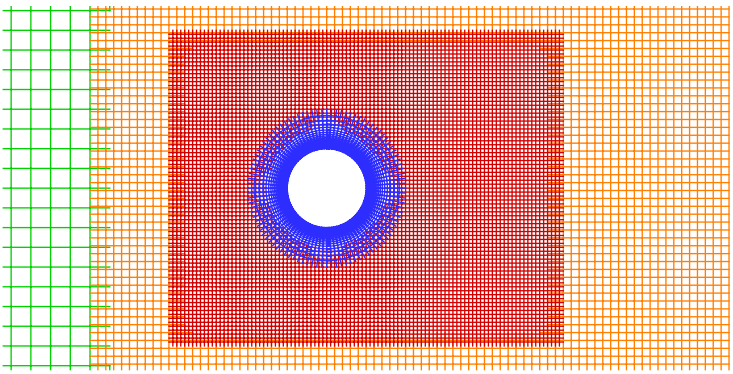

Figure 18. Partial view of the overset grid M1 for flow past a circular cylinder. The overset grid consists of four overlapping and embedded grid systems.

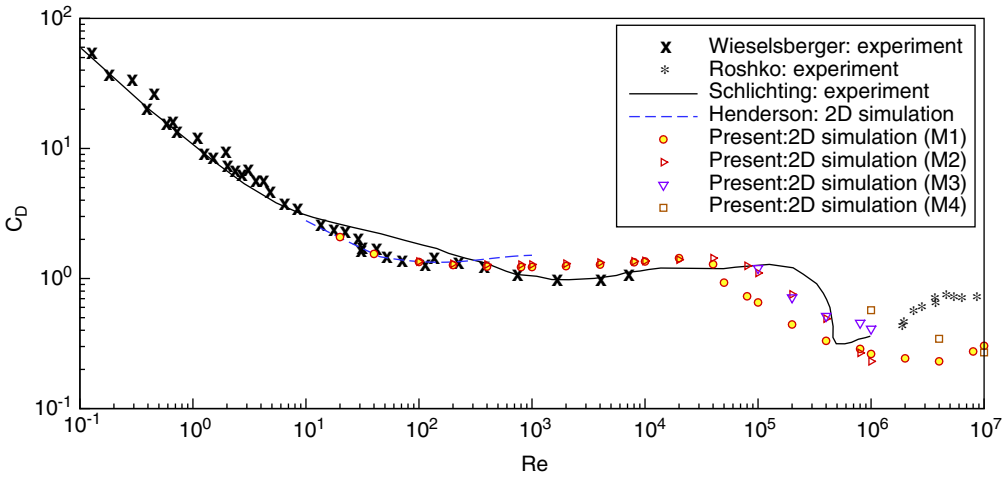

Figure 19. Drag coefficient for a smooth cylinder as a function of Reynolds number.

for details. The information exchange between grid components is mass conservative and of Dirichlet/Dirichlet type by linear Lagrange interpolation at the fringes.

The temporal terms are discretized by the generalized α-method (GAM) family of approximations [27, 28], which retain second-order accuracy in time. Simulations were performed using time-step sizes of $\Delta t = 0.050, 0.020, 0.010$ and 0.005 at the highest Reynolds numbers—to ensure time-step-size-independent solutions.

For each Reynolds number considered the flow is started with initial fields provided by a lower Reynolds number solution, repeatedly decreasing the time-step size until a time-step-size-independent solution is achieved. For selected cases, the simulations were repeated with free-stream initial conditions, to verify initial-condition-independent solutions.

Figure 19 shows the computed *Drag vs Reynolds number* data, alongside data from experimental measurements of Wieselsberger [29], high Reynolds number measurements of Roshko [30], and the well-known experimental curve-fit of Schlichting [31]. Also plotted

Copyright © 2005 John Wiley & Sons, Ltd.

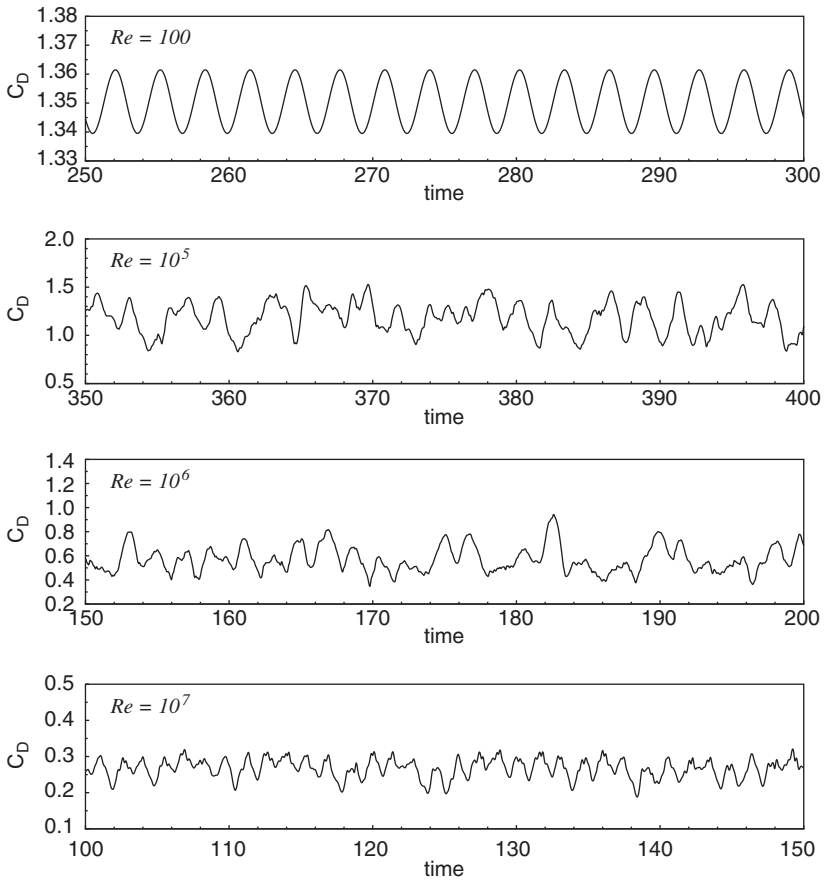

Figure 20. Time history of drag coefficient for increasingly higher Reynolds number.

are the two-dimensional numerical simulation results of Henderson [25], who obtained results up to $Re = 1000$.

The average drag coefficients were determined from statistically representative samples of instantaneous drag recordings; collected over an interval of 10 000 time steps once the flow field was fully developed. We see very good qualitative agreement with the experimental measurements throughout the entire Reynolds number range considered, and are able to predict the drag crisis that occurs during critical transition. Plots of the time history of instantaneous drag coefficient at various Reynolds numbers are shown in Figure 20.

No turbulence model or sub-grid scale model was used for the simulations, so in essence they were ran as direct-numerical simulations, although we do not claim them as such—because the grid was not fine enough to resolve medium and small scales in the far-wake. However, for the purposes of this study it is sufficient to resolve the near-wake flow field, so that accurate instantaneous drag and lift forces may be computed.

Copyright © 2005 John Wiley & Sons, Ltd.

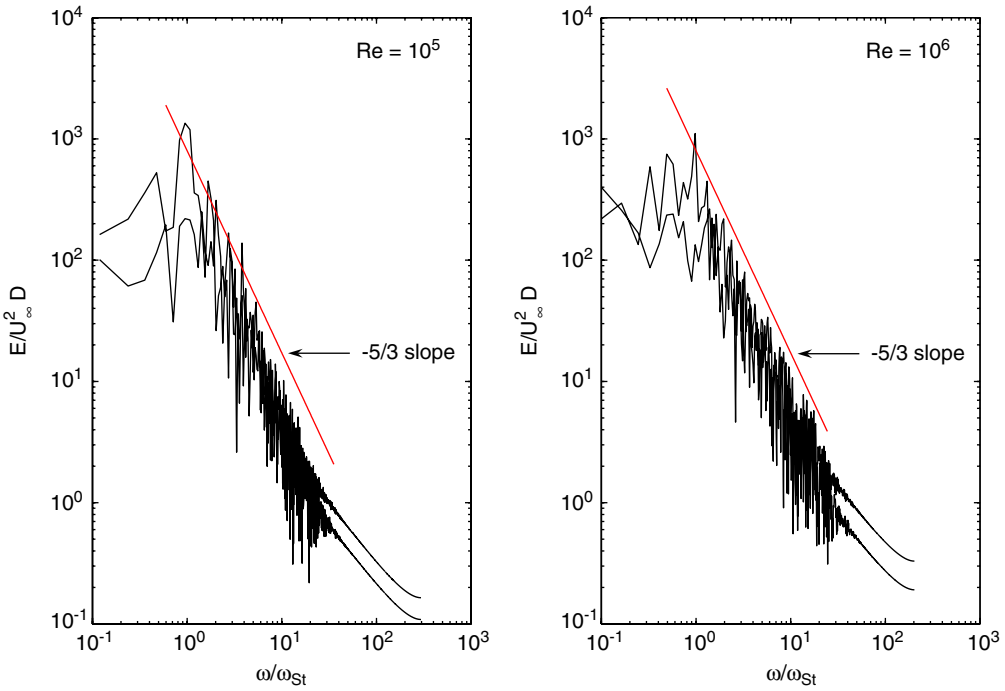

Figure 21. One-dimensional energy spectra 0.25 cylinder diameters away from the base of the cylinder for simulations at $Re = 10^5$ and 10^6 using M3 and M4 resolution, respectively.

Plots of the one-dimensional energy spectra of velocity fluctuations recorded 0.25 cylinder diameters from the base of the cylinder are shown in Figure 21 for $Re = 10^5$ and 10^6 using M3 and M4 resolution, respectively. Streamwise and cross-flow velocities were recorded over a time interval of 50 time units and their energy spectra is shown in Figure 21. The frequency is normalized by the dominant shedding frequency, or Strouhal frequency at the corresponding Reynolds number. The energy spectra shows the $-5/3$ slope in the inertial subrange, indicating that the flow in the wake is turbulent and that M3 and M4 resolution is adequate at the corresponding Reynolds number. The grid is able to resolve medium and small scales in the near-wake, with frequencies up to an order of magnitude higher than the dominant frequency.

Our two-dimensional simulations predict an end to the sub-critical regime around $Re = 10^5$, with a corresponding average drag coefficient of $\bar{C}_D = 1.20$ and a Strouhal number of $St = 0.168$. The Strouhal number is defined here as the frequency with the highest energy content (i.e. the dominant shedding frequency), and is obtained from an energy spectra analysis of the time history of the lift coefficient. Experimental measurements of Bearman [32] place the end of the sub-critical regime around $Re = 2 \times 10^5$ with $\bar{C}_D = 1.14$ and $St \approx 0.190$.

As the Reynolds number is increased past $Re = 10^5$, we cross into the critical transition regime where the drag decreases continuously and the Strouhal number was observed to increase. The increase in Strouhal number in this regime is in accordance with the experiments of Bearman [32]. Experimentally measured flow metrics in this regime are widely scattered because of sensitivity to small degrees of free-stream turbulence and surface roughness.

Copyright © 2005 John Wiley & Sons, Ltd.

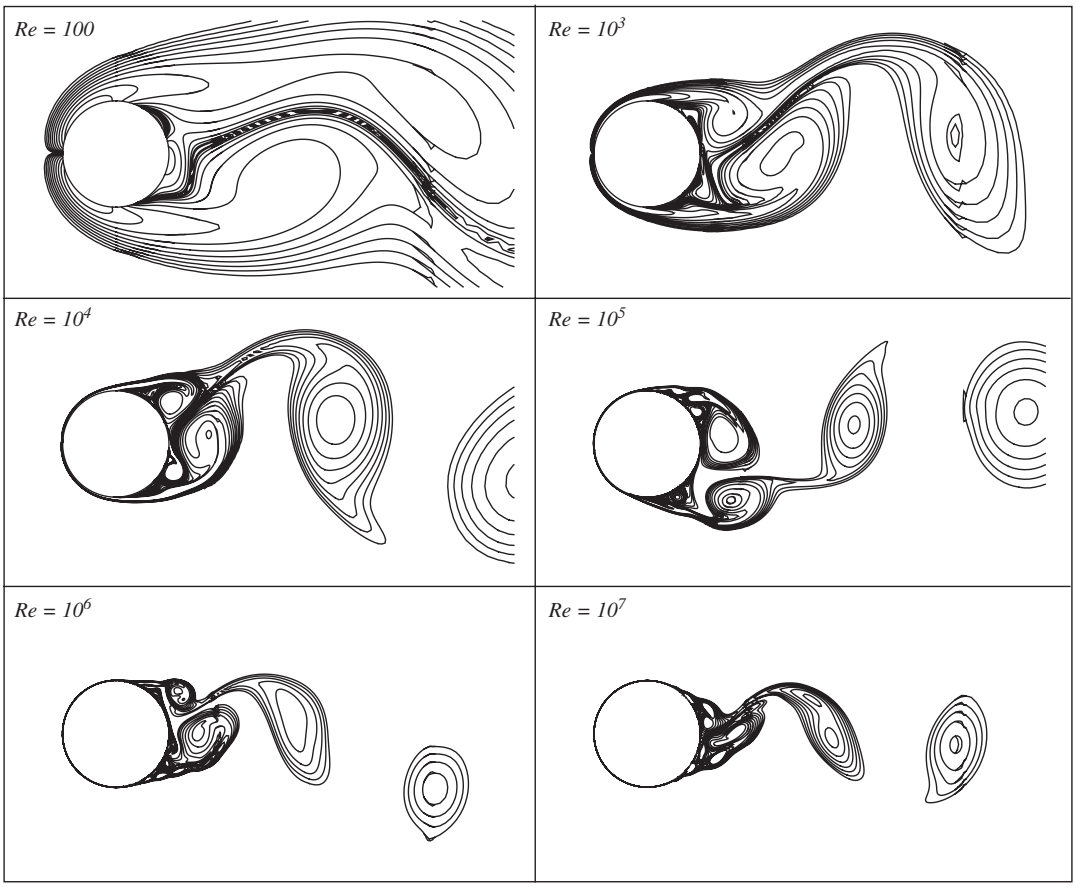

Figure 22. Instantaneous vorticity contours for flow past a circular at increasingly higher Reynolds numbers.

At $Re = 10^6$ we have reached the super-critical regime, where the predicted flow metrics are $\bar{C}_D = 0.571$ and $St = 0.240$. Experimentally measured values at this Reynolds number [30] are in the range $\bar{C}_D \approx 0.20–0.40$ and $St \approx 0.35–0.45$.

In the post-critical regime, measurements of Roshko [30] indicate a drag recovery up to $\bar{C}_D \approx 0.70$ at $Re = 10^7$, with $St \approx 0.27$. Our two-dimensional simulations did not capture such a recovery. At $Re = 10^7$, we predict $\bar{C}_D = 0.270$ and $St = 0.344$. Simulations using the Reynolds-averaged Navier–Stokes (RANS) equations in conjunction with a two-layer k–ε turbulence model [33] gave very similar results: $\bar{C}_D = 0.257$ and $St = 0.40$. We conjecture that the phenomena is due to three-dimensional effects, not accounted for in our simulations.

Figure 22 shows instantaneous vorticity contours for the range of Reynolds numbers considered. The drag crisis is accompanied by a narrowing of the wake, which may be appreciated from the plots. Even though the vorticity field is post-computed from the velocity field, independently in each grid component, we see smooth transitions between grid components. Some

Copyright © 2005 John Wiley & Sons, Ltd.

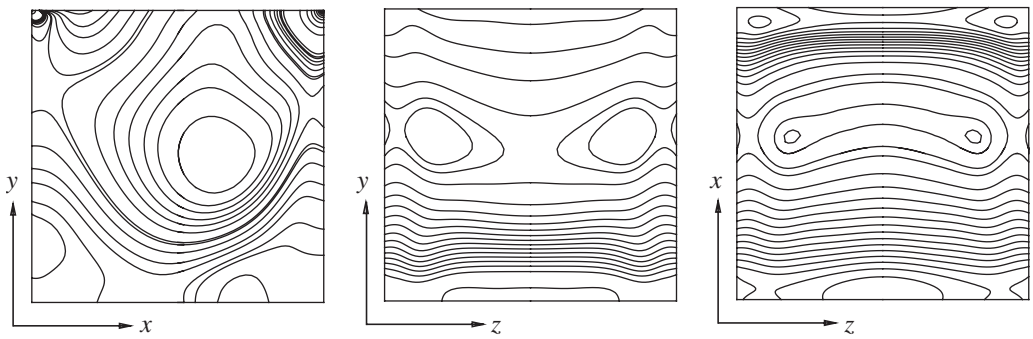

Figure 23. Pressure contours on the planes $z = 0.5$, $x = 0.5$, and $y = 0.5$ for $Re = 1000$: non-uniform mesh solution.

noise is evident where transition to the far-wake grid component occurs, and is due to the abrupt change in length scales used to post-compute the vorticity.

This benchmark problem demonstrates the robustness of the formulation with respect to high Reynolds number flows. Specifically, by robustness, we mean that even when using coarse meshes (such as M1) the procedure is stable and yields physically meaningful results at high Reynolds numbers. These coarse-level results are useful, as they provide general information of the flow field and may be used to design refined meshes for subsequent simulations. As the mesh is refined more features are resolved and overall accuracy improves.

5.6. *Three-dimensional lid-driven cavity flow*

Next, we consider the three-dimensional flow of an incompressible fluid bounded in a cubic enclosure, $\bar{\Omega} = [0, 1] \times [0, 1] \times [0, 1]$, where the flow is driven by the translation of the top x–z-plane. It has been established that, up to $Re = 3200$, the flow is symmetric about the plane $z = 0.5$ [34, 35]. We therefore model only half the domain, and consider uniform and non-uniform meshes consisting of $81 \times 81 \times 41$ nodes.

The Reynolds numbers considered here are 100, 400 and 1000, for which it has been well established that a steady-state solution exists. The boundary conditions are as follows: $u = v = w = 0$ on all solid walls, $p = 0$ at a point, and $u = 1$, $v = w = 0$ on the top-driven surface ($y = 1.0$). Symmetry conditions are applied on the symmetry plane ($z = 0.5$).

The simulations were performed as time accurate, with an impulsive start of the lid at $t = 0$. The impulsive start follows the hyperbolic tangent distribution, $u_{\text{lid}}(t) = \tanh(t)$, allowing for a fast but at the same time smooth start-up. Steady-state was declared when the normalized difference of velocities between two consecutive time steps was below 10^{-5}. At steady-state the L_1 norm of the momentum residuals was below 10^{-3} and the L_∞ norm below 10^{-6} for both uniform and non-uniform meshes.

Figure 23 shows computed pressure contours on the three mid-planes: $z = 0.5$, $x = 0.5$, and $y = 0.5$, at $Re = 1000$. Figure 24 shows computed u-velocity profiles along the vertical mid-line of the plane $z = 0.5$ for the range of Reynolds numbers considered. We see good agreement with tabulated data from published results by Jiang *et al.* [35], who used a least-squares finite element formulation with a non-uniform $50 \times 52 \times 25$ mesh of tri-linear elements.

Copyright © 2005 John Wiley & Sons, Ltd.

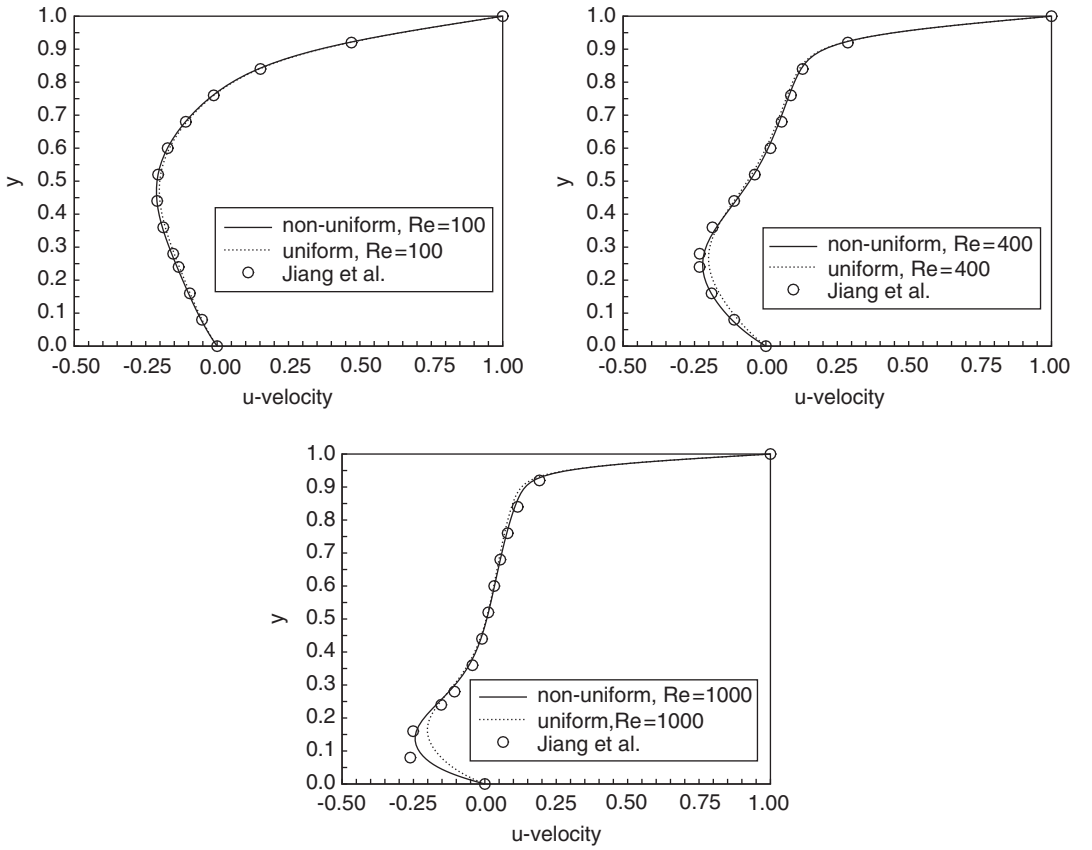

Figure 24. Profiles of u-velocity along the vertical mid-line of the plane $z = 0.5$. Comparison with tabulated values from the published results of Jiang *et al.* [35].

5.7. Vortex-induced vibrations of a circular cylinder

In this last numerical example, we consider flow past a circular cylinder undergoing vortex-induced vibrations (VIV) at high Reynolds number. Our intent is to demonstrate the capabilities of the formulation to simulate such complex physics, and thus we do not present or review in detail basic concepts of the VIV of structures, for which the interested reader is referred to Reference [36].

Long cylindrical risers are used for deep-water extraction of petroleum and natural gas. The flow of seawater around these long cylinders is subject to vortex shedding. If the vortex shedding frequency 'locks-in' to one of the natural frequencies of the riser, the cylinder may undergo severe VIV causing structural fatigue or even failure. Thus, the study of cylinders undergoing VIV is of practical importance in marine and offshore research.

The prediction and simulations of such flows has attracted the attention of experimentalists and CFD practitioners. Conditions experienced by the risers correspond to high Reynolds number flows, with low mass ratio, and low damping. Numerical studies thus far are unable

Copyright © 2005 John Wiley & Sons, Ltd.

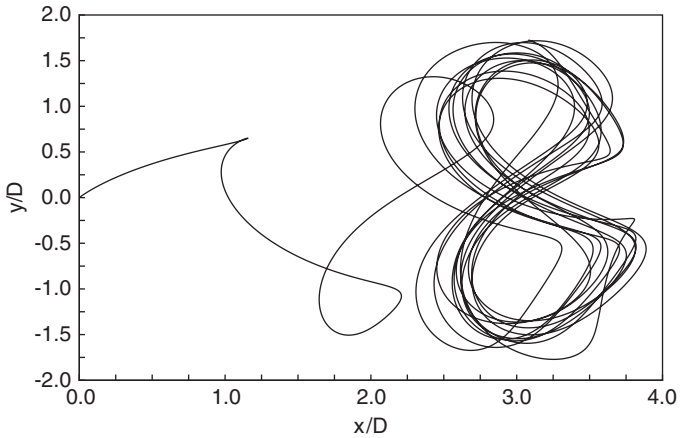

Figure 25. x–y response showing a 'figure-eight' pattern due to VIV of the circular cylinder.

to simulate realistic flow conditions due to low maximum Reynolds numbers limitations of the discretization procedures, and have been limited to mainly single degree-of-freedom (dof) motions. Here, we consider a two-dimensional simulation using typical (realistic) flow conditions experienced by a riser, corresponding to $Re = 1 \times 10^5$, $m^* = 1.0$, $m^* \zeta^* = 0.005$, $U^* = 6.055$, and allowing for 2-dof motions. The dimensionless parameters m^*, ζ^*, and U^* are the structural mass ratio, damping ratio, and reduced velocity, respectively [36].

The problem at hand is essentially a fluid-structure interaction problem, where the cylinder moves as a rigid body in the flow field. The computational domain is the overset (Chimera) grid, consisting of four overlapping and embedded grid systems, used for the stationary cylinder computations. The grid components $\bar{\Omega}_3^h$ and $\bar{\Omega}_4^h$ (with M3 resolution) are allowed to move on the background meshes $\bar{\Omega}_1^h$ and $\bar{\Omega}_2^h$. The ability of the overset grids to move freely on fixed background meshes *eliminates* the overheads of grid re-generation and/or mesh distortion monitoring, and allows for arbitrarily large motions of the structure on the fluid mesh. The grid component $\bar{\Omega}_2^h$ is expanded to dimensions $[-4.0, 10.0] \times [-6.0, 6.0]$, in view of the possibility of large VIV motions.

Given the instantaneous drag and lift forces acting on the cylinder surface (from the fluid-flow solution), the equations of motion governing the x- and y-displacements are integrated in time using a fourth-order Runge–Kutta scheme to determine the instantaneous response of the cylinder. In dimensionless form, the equations of motion are

$$\ddot{y} + \frac{4\pi\zeta^*}{U^*}\dot{y} + \left(\frac{2\pi}{U^*}\right)^2 y = \frac{2}{\pi}\frac{C_{\mathrm{L}}(t)}{m^*}, \quad \dot{y}(0) = y(0) = 0.0$$

$$\ddot{x} + \frac{4\pi\zeta^*}{U^*}\dot{x} + \left(\frac{2\pi}{U^*}\right)^2 x = \frac{2}{\pi}\frac{C_{\mathrm{D}}(t)}{m^*}, \quad \dot{x}(0) = x(0) = 0.0$$

The cylinder is first held stationary until the shedding has reached full strength—at which point the cylinder is 'released' and allowed to respond to the flow field. Figure 25 shows the

Copyright © 2005 John Wiley & Sons, Ltd.

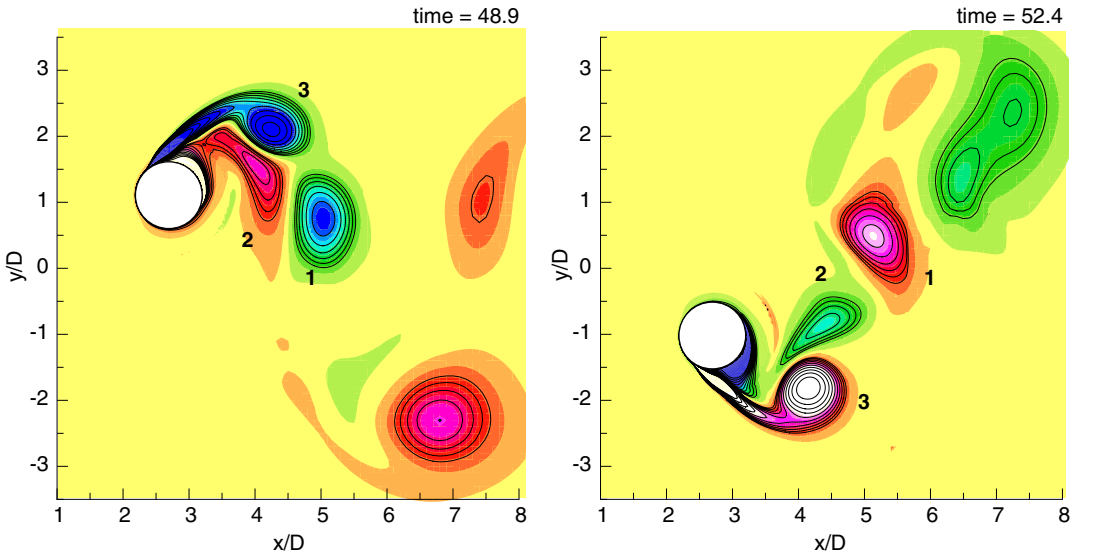

Figure 26. Instantaneous vorticity contours for cylinder undergoing VIV motions, depicting the 2T mode of vortex shedding.

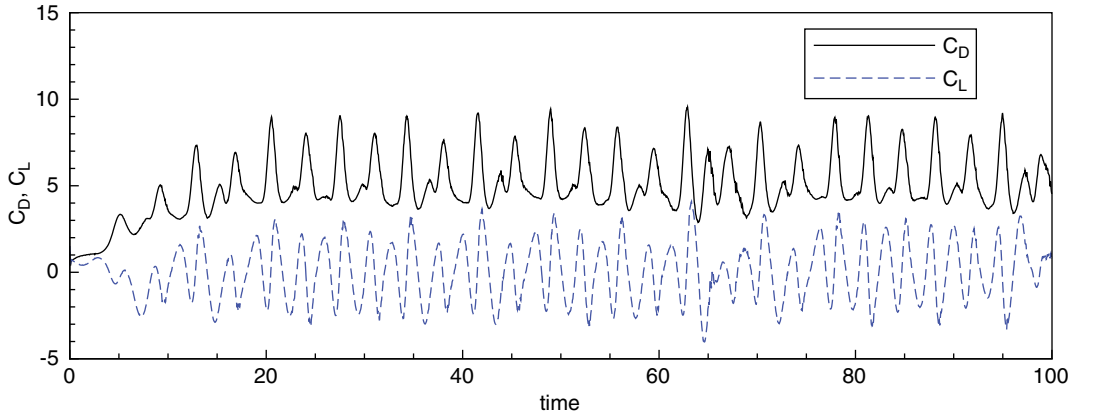

Figure 27. Time history of drag and lift coefficients for cylinder undergoing VIV.

x–y response of the cylinder for $t \in [0, 100]$, where time is implicit in the plot. The response displays average peak-to-peak cross-stream amplitudes of 3.0 cylinder diameters. There is also strong in-line motion with average peak-to-peak amplitudes of 1.0 cylinder diameters. The response is remarkably stable and corresponds to a 'figure-eight' pattern which was maintained throughout the simulation time $t \in [0, 500]$.

In accordance with experiments of Williamson and Jauvtis [37] for 2-dof VIV of circular cylinders with low mass and damping, our simulations indicate that the cylinder sheds

Copyright © 2005 John Wiley & Sons, Ltd.

two triplets of vortices per cycle of body motion. Figure 26 shows the two triplets of vortices shed near the peaks of the cycle. This new mode of vortex shedding has been named the 2T mode by Williamson and Jauvtis [37] and is a signature of the markedly different system dynamics for light bodies undergoing 2-dof VIV motions.

In addition to the interesting body dynamics, a pronounced increase in the drag coefficient is observed. The time history of the drag and lift coefficients is shown in Figure 27. The increase in drag is attributed to the strong in-line motion of the cylinder and is due to the fluid that must be displaced by the cylinder when moving against the oncoming free stream.

6. SUMMARY AND CONCLUDING REMARKS

We presented a collocation-type local-analytic-based discretization procedure for incompressible flows, where interpolants for the velocity components are obtained from local analytic solutions of the linearized momentum equations, and the pressure–velocity coupling is achieved by a discrete projection method. The interpolants retain zeroth- and first-order consistency and the discretization was shown to be asymptotically second-order accurate for velocities and pressure.

Numerical solutions of well-established verification and validation benchmarks were presented to show the robustness of the formulation with respect to (1) strong mesh skews, (2) high Reynolds number flows, and (3) high aspect ratio cells. Numerical examples presented included, two-dimensional flow past a stationary circular cylinder for Reynolds number up to 1×10^7, and flow past a circular cylinder undergoing vortex-induced vibrations at $Re = 1 \times 10^5$.

We believe the formulation represents an attractive alternative to the well-established finite-difference, control-volume, and finite element formulations. The formulation shows remarkable robustness with respect to high Reynolds number flows, where other formulations break down due to numerical instabilities.

APPENDIX A: SOLUTION BY SEPARATION OF VARIABLES

In this appendix we give details of the procedures by which an analytic solution to the two-dimensional advection–diffusion equation can be obtained by the method of separation of variables. Consider the two-dimensional advection–diffusion equation for a generic transported scalar $\phi(x, y)$, in the rectangular domain shown in Figure 1

$$\frac{\partial^2 \phi}{\partial x^2} + \frac{\partial^2 \phi}{\partial y^2} = 2A \frac{\partial \phi}{\partial x} + 2B \frac{\partial \phi}{\partial y} + S \tag{A1}$$

where A, B and S are known constants. In Figure 1 we identify the nodes using compass notation, i.e. north, south, east, west, northwest, etc., this will be an aid in the presentation of the solution procedures.

We construct appropriate boundary data by studying the natural solution for Equation (A1):

$$\phi(x, y) = C_0 e^{2(Ax+By)} + C_1(Ay - Bx) + C_2 - \frac{S}{2(A^2 + B^2)}(Ax + By) \tag{A2}$$

Copyright © 2005 John Wiley & Sons, Ltd.

The first three terms in the solution satisfy the homogeneous part of (A1), the last term is the particular solution of (A1). Next, we define $\tilde{\phi}$ as

$$\tilde{\phi} = \phi + \frac{S}{2(A^2 + B^2)}(Ax + By) \tag{A3}$$

Substituting for ϕ from Equation (A3) into Equation (A1), we see that $\tilde{\phi}$ satisfies the homogeneous equation

$$\left(\frac{\partial^2 \tilde{\phi}}{\partial x^2} + \frac{\partial^2 \tilde{\phi}}{\partial y^2}\right) = 2A\frac{\partial \tilde{\phi}}{\partial x} + 2B\frac{\partial \tilde{\phi}}{\partial y} \tag{A4}$$

The natural solution (A2) suggests that exponential and linear functions in terms of three nodal values on each boundary may be employed to obtain boundary conditions for the element considered. For example, the north boundary condition where y is fixed can be approximated by

$$\tilde{\phi}_{\mathrm{N}}(x) = a_{\mathrm{N}}(\mathrm{e}^{2Ax} - 1) + b_{\mathrm{N}}x + c_{\mathrm{N}} \tag{A5}$$

where

$$\begin{aligned} a_{\mathrm{N}} &= \frac{\tilde{\phi}_{\mathrm{NE}} + \tilde{\phi}_{\mathrm{NW}} - 2\tilde{\phi}_{\mathrm{NC}}}{4\sinh^2 Ah} \\ b_{\mathrm{N}} &= \frac{\tilde{\phi}_{\mathrm{NE}} - \tilde{\phi}_{\mathrm{NW}} - \coth Ah(\tilde{\phi}_{\mathrm{NE}} + \tilde{\phi}_{\mathrm{NW}} - 2\tilde{\phi}_{\mathrm{NC}})}{2h} \\ c_{\mathrm{N}} &= \tilde{\phi}_{\mathrm{NC}} \end{aligned} \tag{A6}$$

The boundary conditions for south, east, and west sides can be similarly approximated by exponential and linear boundary functions as follows:

$$\tilde{\phi}_{\mathrm{S}}(x) = a_{\mathrm{S}}(\mathrm{e}^{2Ax} - 1) + b_{\mathrm{S}}x + c_{\mathrm{S}}$$

$$\tilde{\phi}_{\mathrm{E}}(y) = a_{\mathrm{E}}(\mathrm{e}^{2By} - 1) + b_{\mathrm{E}}y + c_{\mathrm{E}}$$

$$\tilde{\phi}_{\mathrm{W}}(y) = a_{\mathrm{W}}(\mathrm{e}^{2By} - 1) + b_{\mathrm{W}}y + c_{\mathrm{W}}$$

where the coefficients a_{S}, b_{S}, etc. can be expressed in terms of the nodal values along each boundary in a way similar to that for a_{N}, b_{N}, and c_{N} in Equation (A6). Next, we introduce a change of variable

$$\tilde{\phi} = w\,\mathrm{e}^{Ax+By} \tag{A7}$$

and Equation (A4) takes the following form:

$$w_{xx} + w_{yy} = (A^2 + B^2)w \tag{A8}$$

Copyright © 2005 John Wiley & Sons, Ltd.

subject to the 'transformed' boundary conditions

$$w_{\mathrm{N}}(x) = \mathrm{e}^{-Bk}[a_{\mathrm{N}}\mathrm{e}^{Ax} + b_{\mathrm{N}}x\mathrm{e}^{-Ax} + (c_{\mathrm{N}} - a_{\mathrm{N}})\mathrm{e}^{-Ax}] \tag{A9}$$

$$w_{\mathrm{S}}(x) = \mathrm{e}^{Bk}[a_{\mathrm{S}}\mathrm{e}^{Ax} + b_{\mathrm{S}}x\mathrm{e}^{-Ax} + (c_{\mathrm{S}} - a_{\mathrm{S}})\mathrm{e}^{-Ax}] \tag{A10}$$

$$w_{\mathrm{E}}(y) = \mathrm{e}^{-Ah}[a_{\mathrm{E}}\mathrm{e}^{By} + b_{\mathrm{E}}y\mathrm{e}^{-By} + (c_{\mathrm{E}} - a_{\mathrm{E}})\mathrm{e}^{-By}] \tag{A11}$$

$$w_{\mathrm{W}}(y) = \mathrm{e}^{Ah}[a_{\mathrm{W}}\mathrm{e}^{By} + b_{\mathrm{W}}y\mathrm{e}^{-By} + (c_{\mathrm{W}} - a_{\mathrm{W}})\mathrm{e}^{-By}] \tag{A12}$$

Equation (A8) can be solved by the method of separation of variables, by further dividing it into four simpler problems with each of them containing one non-homogeneous and three homogeneous boundary conditions. The solution would then be a superposition of the solutions of the four simpler problems:

$$w(x, y) = w^{\mathrm{N}}(x, y) + w^{\mathrm{S}}(x, y) + w^{\mathrm{E}}(x, y) + w^{\mathrm{W}}(x, y) \tag{A13}$$

The solution, $w(x, y)$, of Equation (A13), has the following form:

$$\begin{aligned} w(x, y) = &\sum_{n=1}^{\infty} C_n^1 \sinh[\mu_n^h(y + k)] \sin[\lambda_n^h(x + h)] + \sum_{n=1}^{\infty} C_n^2 \sinh[\mu_n^h(y - k)] \sin[\lambda_n^h(x + h)] \\ &+ \sum_{n=1}^{\infty} C_n^3 \sinh[\mu_n^k(x + h)] \sin[\lambda_n^k(y + k)] + \sum_{n=1}^{\infty} C_n^4 \sinh[\mu_n^k(x - h)] \sin[\lambda_n^k(y + k)] \end{aligned} \tag{A14}$$

with

$$\lambda_n^h = \frac{n\pi}{2h}, \quad \mu_n^h = \sqrt{A^2 + B^2 + (\lambda_n^h)^2}$$

$$\lambda_n^k = \frac{n\pi}{2k}, \quad \mu_n^k = \sqrt{A^2 + B^2 + (\lambda_n^k)^2}$$

and $\tilde{\phi}(x, y)$ can be immediately obtained from Equation (A7).

To develop expressions for $\tilde{\phi}(0, 0) = \tilde{\phi}^0 = w(0, 0)$, the local analytic solution, Equation (A14), is evaluated at point P, $(x, y) = (0, 0)$ in Figure 1. At point P, the sine functions in Equation (A14) can be decomposed as follows:

$$\sin\left(\frac{n\pi}{2}\right) = \begin{cases} 0 & \text{if } n = 2m \\ -(-1)^m & \text{if } n = 2m - 1 \end{cases} \tag{A15}$$

Since we are interested only in non-zero contributions, Equation (A14) simplifies to give coefficients, $\{\alpha_n^0\}_{n=1}^8$, such that

$$\tilde{\phi}(0, 0) = \tilde{\phi}^0 = \sum_{n=1}^{8} \alpha_n^0 \tilde{\phi}_{\mathrm{n}} \tag{A16}$$

Copyright © 2005 John Wiley & Sons, Ltd.

where the coefficients, $\{\alpha_n^0\}_{n=1}^8$, are given by Equation (12). Since $\tilde{\phi}=1$ and $\tilde{\phi}=-Bx+Ay$ are solutions of Equation (A4), and both of them can be represented exactly by the exponential-linear boundary functions (A5) (i.e. zeroth- and first-order consistency requirements are satisfied), we use them to obtain relationships (19) and (20).

For the general case $S\neq 0$, i.e. $\tilde{\phi}\neq\phi$, the local analytic solution can be obtained by substituting $\tilde{\phi}$ of Equation (A3) into Equation (A16), to obtain α_f^0, such that

$$\phi(0,0)=\phi^0=\sum_{n=1}^{8}\alpha_n^0\phi_n+\alpha_f^0 S \tag{A17}$$

In the actual computer implementation, the following simple re-arrangement of Equations (12) and (13) are used to minimize floating-point roundoff and eliminate overflow when the cell Reynolds number is large:

$$\begin{aligned}
\alpha_1^0&=\frac{e^{Ah+Bk}}{4\cosh Ah\cosh Bk}Q, & \alpha_5^0&=\frac{e^{Bk}}{2\cosh Bk}P_a\\
\alpha_2^0&=\frac{e^{-Ah+Bk}}{4\cosh Ah\cosh Bk}Q, & \alpha_6^0&=\frac{e^{-Ah}}{2\cosh Ah}P_b\\
\alpha_3^0&=\frac{e^{-Ah-Bk}}{4\cosh Ah\cosh Bk}Q, & \alpha_7^0&=\frac{e^{-Bk}}{2\cosh Bk}P_a\\
\alpha_4^0&=\frac{e^{Ah-Bk}}{4\cosh Ah\cosh Bk}Q, & \alpha_8^0&=\frac{e^{Ah}}{2\cosh Ah}P_b
\end{aligned} \tag{A18}$$

$$\alpha_f^0=\frac{Pe}{2(A^2+B^2)}\{Ah\tanh Ah(1-P_a)+Bk\tanh Bk(1-P_b)\} \tag{A19}$$

with

$$P_a=4Ah\cosh Ah\cosh Bk\coth AhE_2 \tag{A20}$$

$$P_b=4Bk\cosh Ah\cosh Bk\coth BkE_2' \tag{A21}$$

$$Q=1-P_a-P_b \tag{A22}$$

and, from first-order consistency, P_a and P_b are related by the expression

$$P_a=1+\frac{Ak\coth Ah}{Bh\coth Bk}(P_b-1) \tag{A23}$$

For large cell Reynolds numbers, the series summation is avoided by considering the asymptotic behaviour of P_a and P_b:

$$\text{if } Ak\coth Ah>Bh\coth Bk,\quad P_a=0,\quad P_b=1-Bh\coth Bk/Ak\coth Ah \tag{A24}$$

$$\text{if } Ak\coth Ah<Bh\coth Bk,\quad P_b=0,\quad P_a=1-Ak\coth Ah/Bh\coth Bk \tag{A25}$$

Copyright © 2005 John Wiley & Sons, Ltd.

APPENDIX B: CURVILINEAR COORDINATES

Given a well-defined mapping, $\bar{\Omega}_e \rightleftarrows \hat{\Omega}_e$, from the orthogonal coordinate system (x^i) to the space (ξ^i), where $\hat{\Omega}_e = [-1,1] \times [-1,1]$, the advection–diffusion equation

$$\frac{1}{Pe}\left[\frac{\partial^2 \phi}{\partial x^m \partial x^m}\right] = u_n \frac{\partial \phi}{\partial x^n} + F \tag{B1}$$

can be written as

$$\frac{1}{Pe}\left[g^{mn}\frac{\partial^2 \phi}{\partial \xi^m \partial \xi^n} + \frac{1}{J}\frac{\partial}{\partial \xi^p}(Jg^{mp})\frac{\partial \phi}{\partial \xi^m}\right] = u_n \frac{\partial \xi^m}{\partial x^n}\frac{\partial \phi}{\partial \xi^m} + F \tag{B2}$$

where J is the Jacobian of the transformation,

$$J^2 = \det(g_{ij}), \quad g_{ij} = \frac{\partial x^m}{\partial \xi^i}\frac{\partial x^m}{\partial \xi^j} \tag{B3}$$

g^{ij} is the contravariant metric tensor associated with the mapping

$$g^{ij} = \frac{1}{J^2}(g_{mp}g_{nq} - g_{mq}g_{np}) \tag{B4}$$

with i,m,n and j,p,q in cyclic order, and

$$\frac{\partial \phi}{\partial x^i} = \frac{\partial \xi^l}{\partial x^i}\frac{\partial \phi}{\partial \xi^l} = \frac{1}{J} b_i^l \frac{\partial \phi}{\partial \xi^l} = \frac{1}{J}\left(\frac{\partial x^j}{\partial \xi^m}\frac{\partial x^k}{\partial \xi^n} - \frac{\partial x^k}{\partial \xi^m}\frac{\partial x^j}{\partial \xi^n}\right)\frac{\partial \phi}{\partial \xi^l} \tag{B5}$$

with i,j,k and l,m,n in cyclic order.

The geometric coefficients J, g^{mn}, and b_n^m given by Equations (B3)–(B5), are functions of the coordinates only. When either analytic or numerical transformations are employed their values can be readily evaluated. Also, note that we have only performed a partial transformation of (B1), i.e. the velocity components are still referenced in the Cartesian coordinate system.

A re-arrangement of (B2) yields

$$g^{mn}\frac{\partial^2 \phi}{\partial \xi^m \partial \xi^n} - \left[Pe\frac{\partial \xi^m}{\partial x^n}u_n - \frac{1}{J}\frac{\partial}{\partial \xi^p}(Jg^{mp})\right]\frac{\partial \phi}{\partial \xi^m} = F$$

where F has absorbed the Peclet number. Now, let

$$2a^m = Pe\frac{\partial \xi^m}{\partial x^n}u_n - \frac{1}{J}\frac{\partial}{\partial \xi^p}(Jg^{mp})$$

so that we can write

$$g^{mn}\frac{\partial^2 \phi}{\partial \xi^m \partial \xi^n} - 2a^m \frac{\partial \phi}{\partial \xi^m} = F$$

or equivalently

$$g^{mm}\frac{\partial^2 \phi}{\partial \xi^m \partial \xi^m} - 2a^m \frac{\partial \phi}{\partial \xi^m} = F - 2\left(g^{12}\frac{\partial^2 \phi}{\partial \xi^1 \partial \xi^2} + g^{13}\frac{\partial^2 \phi}{\partial \xi^1 \partial \xi^3} + g^{23}\frac{\partial^2 \phi}{\partial \xi^2 \partial \xi^3}\right)$$

Copyright © 2005 John Wiley & Sons, Ltd.

Now, we define

$$S = F - 2\left(g^{12}\frac{\partial^2\phi}{\partial\xi^1\partial\xi^2} + g^{13}\frac{\partial^2\phi}{\partial\xi^1\partial\xi^3} + g^{23}\frac{\partial^2\phi}{\partial\xi^2\partial\xi^3}\right)$$

and the advection–diffusion equation can be written as

$$g^{mm}\frac{\partial^2\phi}{\partial\xi^m\partial\xi^m} = 2a^m\frac{\partial\phi}{\partial\xi^m} + S \tag{B6}$$

In the following $\xi^1 = \xi$ and $\xi^2 = \eta$. We locally linearize Equation (B6) in $\hat{\Omega}_e = [-1,1]\times[-1,1]$ by taking representative values of the velocity field, source function, and geometric coefficients—say the value at the centre of element P, $(\xi,\eta) = (0,0)$ in Figure 3.

$$g_{\mathrm{P}}^{11}\frac{\partial^2\phi}{\partial\xi^2} + g_{\mathrm{P}}^{22}\frac{\partial^2\phi}{\partial\eta^2} = 2a_{\mathrm{P}}^1\frac{\partial\phi}{\partial\xi} + 2a_{\mathrm{P}}^2\frac{\partial\phi}{\partial\eta} + S_{\mathrm{P}} \tag{B7}$$

Introducing the coordinate stretching functions:

$$\xi^* = \frac{\xi}{\sqrt{g_{\mathrm{P}}^{11}}}, \quad \eta^* = \frac{\eta}{\sqrt{g_{\mathrm{P}}^{22}}}$$

Equation (B7) is simplified to the standard form seen in Equation (A1), i.e.

$$\frac{\partial^2\phi}{\partial\xi^{*2}} + \frac{\partial^2\phi}{\partial\eta^{*2}} = 2A\frac{\partial\phi}{\partial\xi^*} + 2B\frac{\partial\phi}{\partial\eta^*} + S_{\mathrm{P}} \tag{B8}$$

where

$$A = \frac{a_{\mathrm{P}}^1}{\sqrt{g_{\mathrm{P}}^{11}}}, \quad B = \frac{a_{\mathrm{P}}^2}{\sqrt{g_{\mathrm{P}}^{22}}}$$

for a 'stretched' numerical element with dimensions

$$\Delta\xi^* = h = \frac{1}{\sqrt{g_{\mathrm{P}}^{11}}}, \quad \Delta\eta^* = k = \frac{1}{\sqrt{g_{\mathrm{P}}^{22}}}$$

The mixed derivative terms are momentarily absorbed in the source term, S_{P}, so that the method of separation of variables may be used to solve (B8). These terms are subsequently approximated by finite differences and may be brought back to the left-hand side. For orthogonal elements the mixed derivative terms do not exist. For strongly skewed elements these terms are important and may dominate. The reported results for mildly and strongly skewed meshes (Section 5.3) demonstrate that this treatment is satisfactory.

ACKNOWLEDGEMENTS

Computations for the benchmark problem of flow past a circular cylinder were performed using resources of the Texas A&M Super Computer Facility, their support is acknowledged. The support from the Department of Interior, Mineral Management Services (MMS), and the Offshore Technology Research Center (OTRC) is gratefully acknowledged.

Copyright © 2005 John Wiley & Sons, Ltd.

REFERENCES

1. Ferziger JH, Peric M. *Computational Methods for Fluid Dynamics* (2nd edn). Springer: Berlin, 1996.
2. Reddy JN, Gartling DK. *The Finite Element Method in Heat Transfer and Fluid Dynamics* (2nd edn). CRC Press: Boca Raton, FL, 2001.
3. Karniadakis GE, Sherwin SJ. *Spectral/hp Element Methods for CFD*. Oxford University Press: Oxford, 1999.
4. Christie I, Griffith OF, Mitchell AR, Zienkiewicz OC. Finite element methods for second-order differential equations with significant first-order derivatives. *International Journal for Numerical Methods in Engineering* 1976; **10**:1389–1396.
5. Heinrich JC, Huyakorn PS, Zienkiewicz OC. An upwind finite element scheme for two-dimensional convective transport equation. *International Journal for Numerical Methods in Engineering* 1977; **11**:131–143.
6. Brooks AN, Hughes TJR. Streamline upwind/Petrov–Galerkin formulation for convection dominated flows with particular emphasis on the incompressible Navier–Stokes equations. *Computer Methods in Applied Mechanics and Engineering* 1982; **32**:199–259.
7. Hughes TJR, Franca LP, Hulbert GM. A new finite element formulation for computational fluid dynamics: VIII. The Galerkin/least-squares method for advective–diffusive equations. *Computer Methods in Applied Mechanics and Engineering* 1989; **73**:173–189.
8. Jiang BN. *The Least-Squares Finite Element Method*. Springer: New York, 1998.
9. Pontaza JP, Reddy JN. Spectral/*hp* least-squares finite element formulation for the Navier–Stokes equations. *Journal of Computational Physics* 2003; **190**:523–549.
10. Pontaza JP, Reddy JN. Space-time coupled spectral/*hp* least-squares finite element formulation for the incompressible Navier–Stokes equations. *Journal of Computational Physics* 2004; **197**:418–459.
11. Reddy JN. *An Introduction to Nonlinear Finite Element Analysis*. Oxford University Press: Oxford, 2004.
12. Chen HC. Development of finite analytic method for unsteady three-dimensional Navier–Stokes equations. *Ph.D. Dissertation*, The University of Iowa, 1982.
13. Chen CJ, Chen HC. Finite analytic numerical method for unsteady two-dimensional Navier–Stokes equations. *Journal of Computational Physics* 1984; **53**:209–226.
14. Sani RL, Gresho PM. Resume and remarks on the open boundary condition minisymposium. *International Journal for Numerical Methods in Fluids* 1994; **18**:983–1008.
15. Pontaza JP. Formulation and evaluation of finite element discretization schemes for high Reynolds number incompressible fluid flows. *Master of Science Thesis*, Massachusetts Institute of Technology, 2001.
16. Stone HL. Iterative solution of implicit approximations of multidimensional partial differential equations. *SIAM Journal on Numerical Analysis* 1968; **5**:530–558.
17. Chen CJ, Bravo RH, Chen HC, Xu Z. Accurate discretization of incompressible three-dimensional Navier–Stokes equations. *Numerical Heat Transfer* 1995; **27**:371–392.
18. Chen HC, Patel VC, Ju S. Solution of Reynolds-averaged Navier–Stokes equations for three-dimensional incompressible flows. *Journal of Computational Physics* 1990; **88**:305–336.
19. Kovasznay LIG. Laminar flow behind a two-dimensional grid. *Proceedings of the Cambridge Philosophical Society* 1948; **44**:58–62.
20. Sotiropoulos F, Abdallah S. The discrete continuity equation in primitive variable solutions of incompressible flow. *Journal of Computational Physics* 1991; **95**:212–227.
21. Gartling DK. A test problem for outflow boundary conditions—flow over a backward-facing step. *International Journal for Numerical Methods in Fluids* 1990; **11**:953–967.
22. Demirdzic I, Lilek Z, Peric M. Fluid flow and heat transfer test problems for non-orthogonal grids: benchmark solutions. *International Journal for Numerical Methods in Fluids* 1992; **15**:329–354.
23. Jackson CP. A finite-element study of the onset of vortex shedding in flow past variously shaped bodies. *Journal of Fluid Mechanics* 1987; **182**:23–45.
24. Dušek J, Le Gal P, Fraunié P. A numerical and theoretical study of the first Hopf bifurcation in a cylinder wake. *Journal of Fluid Mechanics* 1994; **264**:59–80.
25. Henderson RD. Details on the drag curve near the onset of vortex shedding. *Physics of Fluids* 1995; **7**:2102–2104.
26. Chesshire G, Henshaw WD. Composite overlapping meshes for the solution of partial differential equations. *Journal of Computational Physics* 1990; **90**:1–64.
27. Jansen KE, Whitting CH, Hulbert GM. A generalized α-method for integrating the filtered Navier–Stokes equations with a stabilized finite element method. *Computer Methods in Applied Mechanics and Engineering* 2000; **190**:305–319.
28. Dettmer W, Peric D. An analysis of the time integration algorithms for the finite element solutions of incompressible Navier–Stokes equations based on a stabilised formulation. *Computer Methods in Applied Mechanics and Engineering* 2003; **192**:1177–1226.
29. Wieselsberger C. Neuere Feststellungen uber die Gesetze des Flussigkeits und Luftwiderstands (New findings in the laws of fluid and air resistance). *Physikalische Zeitschrift* 1921; **11**:321–328.

Copyright © 2005 John Wiley & Sons, Ltd.

30. Roshko A. Experiments on the flow past a circular cylinder at very high Reynolds number. *Journal of Fluid Mechanics* 1961; **10**:345–356.
31. Schlichting H. *Boundary-Layer Theory* (7th edn). McGraw-Hill: New York, 1979.
32. Bearman PW. On vortex shedding from a circular cylinder in the critical Reynolds number regime. *Journal of Fluid Mechanics* 1969; **37**:577–585.
33. Chen HC, Patel VC. Near-wall turbulence models for complex flows including separation. *AIAA Journal* 1988; **26**:641–648.
34. Reddy JN. Penalty-finite-element analysis of 3-D Navier–Stokes equations. *Computer Methods in Applied Mechanics and Engineering* 1982; **35**:87–106.
35. Jiang BN, Lin TL, Povinelli LA. Large-scale computation of incompressible viscous flow by least-squares finite element method. *Computer Methods in Applied Mechanics and Engineering* 1994; **114**:213–231.
36. Blevins RD. *Flow-Induced Vibrations* (2nd edn). Van Norstrand: New York, 1990.
37. Williamson CHK, Jauvtis N. A high-amplitude 2T mode of vortex-induced vibration for a light body in XY motion. *European Journal of Mechanics B/Fluids* 2004; **23**:107–114.

Copyright © 2005 John Wiley & Sons, Ltd.